Section 3

Computational studies including new techniques, the effect of varying model resolution, parallel processing

Idealised Tests of the very short range Forecast Model LMK

Michael Baldauf, Jochen Förstner, Peter Prohl
Deutscher Wetterdienst, Kaiserleistraße 42, 63067 Offenbach am Main
E-mail: michael.baldauf@dwd.de, jochen.foerstner@dwd.de, peter.prohl@dwd.de

At the Deutscher Wetterdienst (DWD) the NWP model LMK ('LM Kürzestfrist') is under development since the end of 2003 with the goal to deliver weather forecasts for a very short time range (up to 18 h) with a spatial resolution lying in the meso-γ-scale (about 2.5-3 km). We expect at this resolution that the very coarse scale structures of convective cells can be resolved and severe weather events, connected e.g. with super- and multi cell thunderstorms can be simulated by the model to a certain extent. Additionally effects of more fine scaled topography (severe downslope winds, Föhn storms, ...) can be considered (Doms and Förstner 2004).

The starting point for this development is the nonhydrostatic, compressible model LM ('Lokal-Modell') (Schär et al. 2002), which is in operational use since end of 1999 and which was extended to handle with the higher resolution by several steps. As mentioned, at a resolution of 2.8 km the LMK partly can develop deep convection explicitly. Consequently a full parameterisation of deep convection is not longer needed. But one still needs again a mechanism to transport humidity out of the boundary layer, therefore a parameterisaton for this 'shallow convection' by a simplification of the Tiedtke-scheme is used. Furthermore besides the humidity variables water vapour, cloud water, cloud ice, rain and snow a new ice phase (graupel) with higher sedimentation velocities than snow is needed for the explicit simulation of deep convection (Reinhardt 2005).

In this article we want to concentrate on the improvements of the dynamical core. Instead of the Leapfrog-time-splitting method used in LM a 2-timestep TVD-Runge-Kutta-method of 3rd order was used (Förstner and Doms 2004). This allows the use of advection schemes of higher spatial order (here: upwind 5th order) at relatively high Courant numbers. This dynamical core was tested in several studies.

The test case of a non-linear 2-dim. density current, generated by a falling cold bubble, was proposed 1990 at the 'Workshop on Numerical Methods for solving linear flow problems' and is e.g. described in Straka et al. (1993). In a steady, dry adiabatic stratified atmosphere with $\Theta = 300$ K, an elliptic cold bubble is set with a maximum extension of 8 km horizontally and 4 km vertically, centered in 3 km height and up to 15 K colder than the surrounding atmosphere. The generation of arbitrary small structures is suppressed by an artificial diffusion ($K = 75$ m^2/s). By this scale-limiting diffusion a grid-convergent solution can be found which was calculated by Straka et al. (1993) based on an ongoing reduction of the grid resolution with an elementary solver. This reference solution is shown after 900 s in figure 1 (left, above). One recognizes especially the propagation of a bow front and the generation of Kelvin-Helmholtz-instabilities connected with the density current. In figure 1 (left, below) the comparison with the Runge-Kutta 3rd order time-integration scheme and a resolution of $\Delta x = 50$ m is presented.

A further test with a 2-dimensional flow over a bell-shaped mountain of 100 m height and a half width of 4 grid spacings was performed and compared to the analytic solution. In figure 1, right, an isothermal stratification with $T_0 = 285.15$ K, an incoming flow with $U = 10$ m/s and a resolution of $\Delta x = 7$ km was used. In the simulation with the new dynamic core a considerably bigger time step of 72 s is used compared to the Leapfrog-scheme used in LM (40 s) and the solution compares at least equally well with the analytical one as the results for the Leapfrog core. This is especially the case in the lower half of the domain. The discrepancies in the upper half are mainly due to the upper boundary condition where a damping layer is used.

In a third idealized study the flow over a bell-shaped mountain with superimposed variations

$$h(x) = h_0 \exp\left[-\left(\frac{x}{a}\right)^2\right] \cos^2\left(\frac{\pi x}{\lambda}\right)$$

with $h_0 = 250$ m, $a = 5$ km and $\lambda = 3$ km is simulated. The results for two different height coordinates — SLEVE (Schär et al. 2002) and the normal Gal-Chen formulation — are shown in figure 2. This is a good test of the formulation of the metric terms in terrain-following coordinates (Klemp et al. 2003)

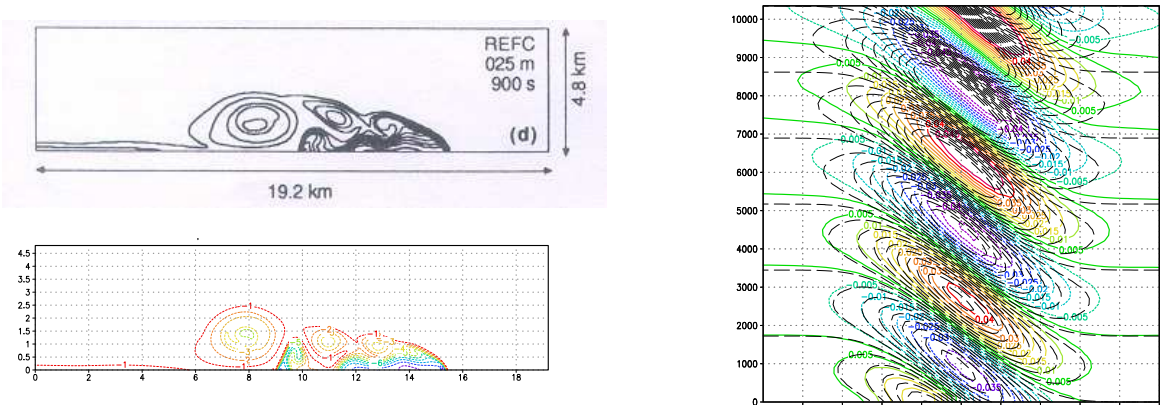

Figure 1: *Vertical cross sections for:*
Left side: $\Theta' = \Theta - \Theta_0$ *for the density current test after 900 s. above: reference solution by Straka et al. (1993), below: LMK solution. It is only shown the right half of this symmetric flow.*
Right side: vertical wind velocity w for a 2D isothermal flow over a mountain after a simulation time of 30 h. The analytic solution is given in thin dashed contours.

especially at the lower boundary, since inconsistent treatment would lead to small scale distortions of the wave structure higher up in the atmosphere.

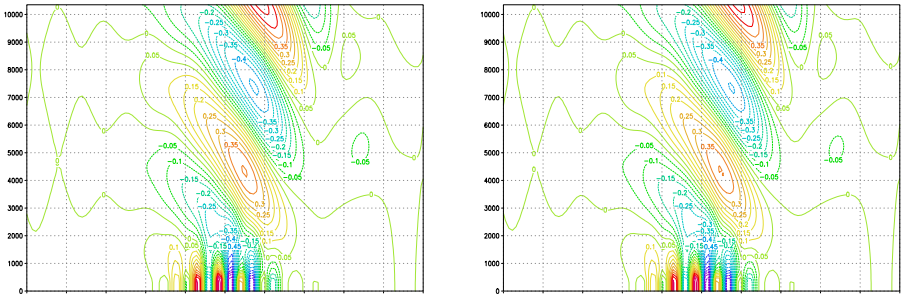

(a) SLEVE coordinate. (b) Gal-Chen coordinate.

Figure 2: *Vertical cross section of w for a 2D flow after a simulation time of 24 h. Incoming flow:* $U = 10$ *m/s; stratification:* $N = 0.01\ s^{-1}$ – $T_0 = 285.15$ *K.* $\Delta x, \Delta y = 500$ *m.*

References

Doms, G. and Förstner, J., 2004: Development of a NWP System for Very Short-Range Forecasts *WGNE Blue Book*, http://www.cmc.ec.gc.ca/rpn/wgne/

Doms, G., and Schättler, U., 2002: A description of the Nonhydrostatic Regional Model LM, http://cosmo-model.cscs.ch/cosmoPublic/

Förstner, J. and Doms, G., 2004: Runge-Kutta Time Integration and High-Order Spatial Discretization - a New Dynamical Core for the LMK *WGNE Blue Book*, http://www.cmc.ec.gc.ca/rpn/wgne/

Klemp, J. B., W. C. Skamarock, and O. Fuhrer (2003). Numerical consistency of metric terms in terrain-following coordinates. *Mon. Wea. Rev. 131*, 1229–1239.

Reinhardt, T., 2005: A prognostic Graupel Microphysics scheme for high-resolution NWP *WGNE Blue Book*, http://www.cmc.ec.gc.ca/rpn/wgne/

Schär, C., D. Leuenberger, O. Fuhrer, D. Lüthi, and C. Girard (2002). A new terrain-following vertical coordinate formulation for atmospheric prediction models. *Mon. Wea. Rev. 130*, 2459–2480.

Straka, J.M., Wilhelmson, R.B., Wicker, L.J., Anderson, J.R. and Droegemeier, K.K., 1993:, Numerical solutions of a non-linear density current - a benchmark ..., *Int. J. Num. Meth. Fluids*, 17, 1-22

Study of different formulations for continuity equation in the SL-AV NWP model

Nickolay Bogoslovskii, Mikhail Tolstykh
Institute of Numerical Mathematics, Russian Academy of Sciences
8 Gubkina st. 119991 Moscow Russia
Email: dorgun@mail.ru, tolstykh@inm.ras.ru

The SL-AV (semi-Lagrangian, absolute vorticity) model [1] is currently used at the Russian Hydrometeorological Research Centre to produce 10-days forecasts in parallel with the operational spectral Eulerian model. The resolution of the SL-AV model is 0.9 degrees in longitude, 0.72 degrees in latitude, 28 vertical sigma-levels.

In certain meteorological situations, the orographic resonance can be seen in model forecasts, despite all the undertaken measures known from literature (Eulerian treatment of orography [2], SETTLS scheme [3]). The model formulated in vertical σ–coordinate employs the continuity equation formulation from [4], which can be written without Tanguay-Ritchie modification [2] as

$$\frac{d\left(\ln p_s\right)}{dt} + D + \frac{\partial \dot{\sigma}}{\partial \sigma} = 0,$$

where D - is the horizontal divergence on σ -surface.

It was decided to study the effect of another formulation of continuity equation. It was changed to the one of the ECMWF model [5]. Adapting it to the sigma-coordinate and SL-AV two-time-level semi-implicit scheme gives

$$\left(1-\sigma_T\right)\left(\ln p_s\right)^{n+1} = \sum_{k=1}^{NLEV} \Delta\sigma_k \left\{ \left(\ln p_s\right)^n_{*,2} + \Delta t \left[-\sum_{j=1}^{NLEV} \left(\vec{V}_j \cdot \nabla \ln p_s\right) \Delta\sigma_j + \vec{V}_k \cdot \nabla \ln p_s \right]^{n+1/2} \right.$$
$$\left. - \frac{\Delta t}{2} \left[\left(\sum_{j=1}^{NLEV} \Delta\sigma_j D_j \right)^{n+1} + \left(\sum_{j=1}^{NLEV} \Delta\sigma_j D_j \right)^{n}_{*} \right] \right\}$$

where $\vec{V}$ is the horizontal velocity, *NLEV* - number of vertical levels, the (*n+1/2*)-time level term is discretized along the trajectory with SETTLS scheme; here again the modification [2] is omitted for simplicity, for the same reason temporal decentering is omitted, though both things are present in the actual model.

The discretization of thermodynamic equation still follows [4], however, the term containing sigma-dot on (*n+1*)-th time level now uses its value recalculated at the beginning of the next time step.

To test this modification, two 48-hours forecasts starting from the first of November 2004, 12UTC, were carried out. The initial data are the uninitialized analysis of SL-AV OI-based data assimilation and thus may contain already traces of orographic resonance.

Fig.1 depicts isolines of 48-hours forecast for 500 hPa geopotential in the part of Asia obtained with the “standard” formulation of continuity equation, and Fig. 2 presents the same field obtained with the modified formulation of continuity equation. One can see a sensitivity of the resulting field to the changes in the discretization of continuity equation.

This effect will be studied in more details with two series of assimilation runs and forecasts on their basis using these two formulations of continuity equation.

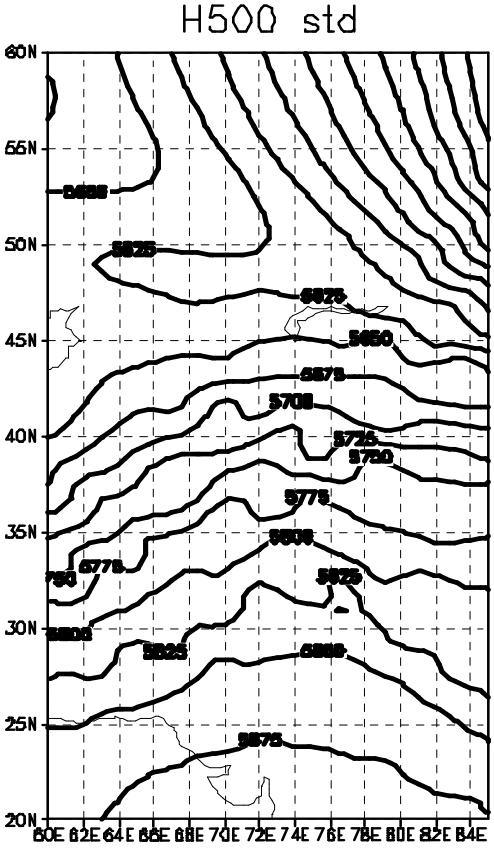

Fig.1 .

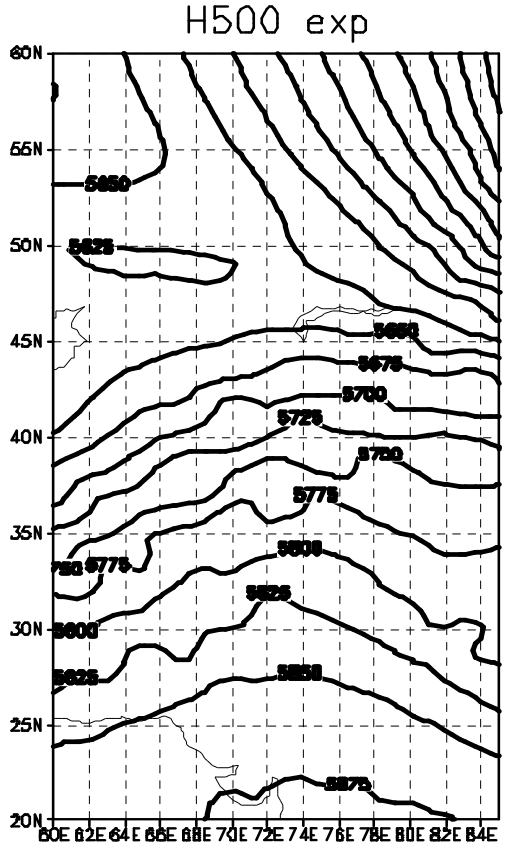

Fig.2.

This work was supported with Russian RFBR grant 04-05-64638.

References

1. Tolstykh M.A. Semi-Lagrangian high-resolution atmospheric model for numerical weather prediction. Russian Meteorology and Hydrology, 2001, N 4, p. 1-9.
2. Ritchie H and Tanguay M.A. A comparison of spatially averaged Eulerian and Semi-Lagrangian treatments of mountains. Mon. Weather Rev., 1996, v. 124, p 167-181.
3. Hortal M. The development and testing of a new two-time-level semi-Lagrangian scheme (SETTLS) in the ECMWF forecast model. Q. J. Roy. Met. Soc., 2002, v. 128, 1671-1688.
4. Bates J.R., Moorthi S., Higgins R.W. A global multilevel atmospheric model using a vector semi-Lagrangian finite-difference scheme. Mon. Weather Rev., 1993, v. 121, p. 244-263.
5. Ritchie H., Temperton C., Simmons A., Hortal M., Davies T., Dent D., Hamrud M. Implementation of the Semi-Lagrangian method in a high-resolution version of the ECMWF forecast model. Mon. Weather Rev., 1995, v. 123, p. 489-514.

The ICON dynamical core project: modelling strategies and preliminary results

Luca Bonaventura, Luis Kornblueh, Erich Roeckner
Max Planck Institut für Meteorologie
Bundesstr. 53, 20146, Hamburg, Germany
e-mail: bonaventura@dkrz.de, kornblueh@dkrz.de, roeckner@dkrz.de

Thomas Heinze, Detlev Majewski, Pilar Ripodas
Deutscher Wetterdienst
Kaiserleistr. 42, 63067, Offenbach, Germany
e-mail: thomas.heinze@dwd.de, detlev.majewski@dwd.de, maria-pilar.ripodas@dwd.de

The ICON project is a joint development effort of MPIfM and DWD to achieve a unified climate and NWP model using geodesic grids. The model under development in the ICON project will use the fully elastic, nonhydrostatic Navier-Stokes equations, which provide a framework that is sufficiently general for meteorological applications on most scales relevant to numerical weather prediction and climate simulation.

As an intermediate step, a semi-implicit discretization for the hydrostatic primitive equations is being developed. The proposed horizontal discretization uses the triangular Delaunay cells of the icosahedral grid as control volumes. It achieves mass and potential enstrophy conservation, thus replicating the results of [2] for standard rectangular C grids. Vector radial basis function interpolation is used to reconstruct a uniquely defined velocity field from the velocity components normal to the cell sides, which are the discrete model variables along with the cell averaged value of the geopotential height. A full description of the horizontal discretization can be found in [1]. The results obtained with a preliminary shallow water implementation on an idealized test case (see e.g. [3]) are shown in figure 1, while the results of a convergence test are shown in figure 2. For this test, a spectral transform model developed at NCAR was used to produce a reference solution. An application of the same technique to an hydrostatic model with local grid refinement option equations for global nonhydrostatic modelling are currently being investigated.

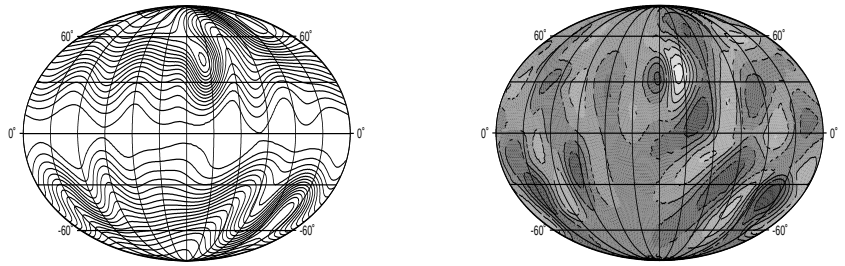

(a) (b)

Figure 1: Height field (a) and relative vorticity field at day 15 for test case 5 of [3], computed by the mass conservative shallow water model on the triangular icosahedral grid with 81920 triangles. Contours spacing is 50 m and 10^{-5} s^{-1}, respectively.

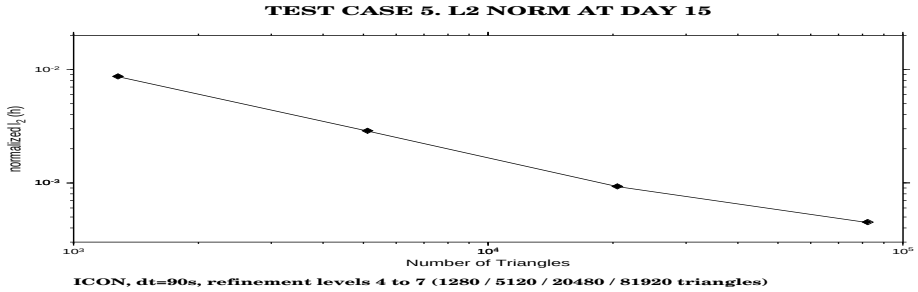

Figure 2: Error on the height field at various spatial resolutions at day 15 for test case 5 of [3].

References

[1] L. Bonaventura. The ICON project: Development of a unified model using triangular geodesic grid. In *Proceedings of the ECMWF Annual Seminar on Development in Numerical Methods for Atmosphere and Ocean Modeling*. ECMWF, 2004.

[2] R. Sadourny. The dynamics of finite difference models of the shallow water equations. *Journal of the Atmospheric Sciences*, 32:680–689, 1975.

[3] David L. Williamson, John B. Drake, James J. Hack, Rüdiger Jakob, and Raul N. Swarztrauber. A standard test set for numerical approximations to the shallow water equations in spherical geometry. *Journal of Computational Physics*, 102:221–224, 1992.

Topographic Rossby Waves in a Z-level ocean model

Dmitry S. Dukhovskoy, Steven L. Morey, and James J. O'Brien
Center for Ocean-Atmospheric Prediction Studies, Florida State University, Tallahassee, Florida, USA, ddmitry@coaps.fsu.edu.

Topographic Rossby waves (TRW) play an important role in the ocean dynamics in regions where the slope of the bottom topography is sufficiently large so as to dominate the β-effect. TRW propagate signals in the ocean along the slopes over large distances [*Oey and Lee*, 2002]. *Pacanowski and Gnanadesikan* [1998] suggested that when the bottom slope is less than the grid cell aspect ratio (Δz/Δx) in a numerical ocean model with a Z-level vertical coordinate, the model does not accurately resolve topography leading to an inaccurate simulation of topographic waves with a modified dispersion relation. It is important to better understand the consequences of the modelers' choices of vertical grids since coarse vertical resolution ocean models can alter the rate and direction of propagation of waves. In this study we examine the ability of Z-level models to accurately simulate topographic waves by conducting model experiments with σ-level (terrain following) and Z-level vertical coordinate systems with different vertical resolutions.

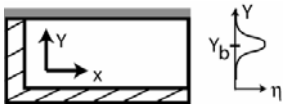

Figure 1. *Model domain. The impulse is imposed at the eastern boundary. Dashed region is a "sponge" domain.*

A long barotropic shelf in the northern hemisphere with variable depth H on an *f*-plane is considered (Figure 1). The width of the shelf is 400 km, and the depth linearly increases offshore from 0 to 400 m. The bottom slope (α) is $1\text{x}10^{-3}$ which is sufficiently large $\left(|\nabla H| > H/R\tan\phi_0\right)$ to dominate the β-effect (R is radius of the Earth) [*LeBlond and Mysak*, 1978]. The horizontal grid spacing is 5 km. The dashed area is a sponge region with a linearly increasing spatial step to prevent the open boundaries from interfering with the solution within the interior of the domain. The simulations are performed with the Navy Coastal Ocean Model (NCOM) [*Martin*, 2000]. The model is initialized at rest and integrated for 20 days. Forcing is applied at the eastern open boundary in the form of a Gaussian sea level anomaly with a dynamically consistent velocity field (Figure 1): $\eta = \eta_0 \exp\left(-\left((y-y_b)^2/0.0225\right)\right)$, where

$$\eta_0 = \begin{cases} 0.18\cdot\exp\left((day-5)^2/2\right), & day < 9 \\ 0, & otherwise \end{cases}$$

, y_b=0.5 is the offshore location of the maximum normalized by the shelf width. The control run is performed with 2 σ levels which, for given slope, realistically resolve the topography (Figure 2a). Then several runs using Z-levels with the number of levels varying from 3 to 40 are performed. Models with coarse vertical resolution significantly alter the topography (Figure 2) and affect the characteristics of topographic waves initiated by the impulse (Figure 3). With very coarse vertical resolution (3 Z-levels) the bottom topography is approximated by several wide steps (Figure 2b) with widths comparable to the barotropic Rossby radius (L=150 km, Ro ~ 600 km). The model produces double Kelvin waves trapped by the partial vertical walls [*LeBlond and Mysak*, 1978] (Figure 3b) artificially created by vertical discretization of the topography. As the vertical resolution increases, double Kelvin waves can not be supported by

Figure 2. *Bottom topography in model experiments with σ-levels (a) and Z-levels (b through h). The number of Z levels increases from (b) to (h): 3, 4, 5, 6, 8, 16, and 40. The ordinate is depth (m) and the abscissa is the offshore distance divided by shelf width.*

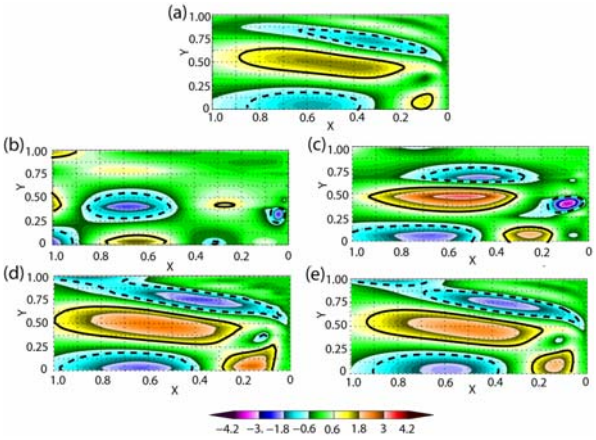

Figure 3. *Snapshots of simulated topographic waves. SSH anomalies (cm) on the 13th day of integration. Solid line contours are drawn at 1 cm, and dashed line contours are -1 cm. The abscissa is the along-shelf distance normalized by the length of the domain (1000 km). The ordinate is as in Figure 2. (a) σ-level model; (b) 3 Z-levels; (c) 5 Z-levels; (d) 16 Z-levels; (e) 40 Z-levels. Note that (d) and (e) are similar to (a).*

narrow steps and the solution approaches propagating TRW similar to those simulated with the σ-level model (compare Figures 3b to 3e with 3a).

Hovmöller diagrams of the crosscorrelation coefficients of the sea surface height (SSH) anomalies along the shelf (Figure 4) are used to estimate the phase velocity of the topographic waves. The crosscorrelation coefficients are calculated between the SSH on the day after the forcing at the eastern boundary has died out and the system reaches quasi-geostrophic balance (8-10th day of the integration) and daily SSH after that day. The estimated phase speed of the TRW simulated with the σ-level model is ~2.5 km/hour. Comparison of the diagrams for the Z-level models with course resolution (Figures 4b – 4e) reveals an obvious and significant modification of the wave. Starting from the model with 8 Z-levels, the solution approaches the σ-level solution (compare Figures 4f-4h with 4a).

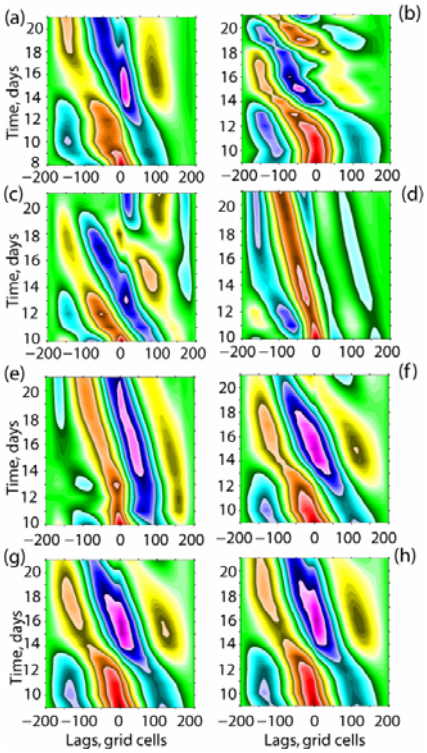

Figure 4. *Hovmöller diagrams of the SSH autocorrelation for 8 experiments using σ-levels (a) and Z-levels (b through h) shown in Figure 2. Note that the solutions using Z-levels approach the σ-level solution (a) as the number of Z-levels increases.*

The obvious conclusion is that Z-level models can accurately reproduce TRWs if the bathymetry is well resolved in the model. Poor vertical resolution leads to an unrealistic representation of the bathymetry, which initiates different waves with different dispersion relations resulting in errors of signal propagation in the model. Future research will focus on establishing the necessary criteria for the resolution of bathymetry in Z-level models for properly simulating TRW. From preliminary results it can be noted that the ratio between the grid cell aspect ratio to the topographic slope discussed earlier may not be a *necessary* criteria for a Z-level model's ability to reproduce TWS. It was previously understood that this ratio should be 1 (as in σ-level models) which necessitates that the number of vertical grid points in most typical Z-level model configurations must be dramatically increased. However these results suggest that the ratio does not need to be 1 (Figures 5). For this domain, even 8 Z levels (with a grid cell aspect ratio 10 times larger than the bottom slope) seem to be enough to reproduce TRW similar to the σ-level model (Figure 4).

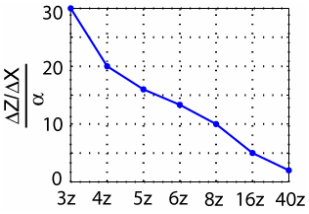

Figure 5. *Ratio of the grid cell aspect ratio and bottom slope for the models with different number of Z levels.*

Acknowledgements

This project was sponsored by the Office of Naval Research Secretary of the Navy grant to James J. O'Brien, and by the NASA Office of Earth Science. Computer time was the FSU Academic Computing and Network Services.

References

LeBlond, P.H., and L.A. Mysak, *Waves in the Ocean*, 602 pp., Elsevier, New York, 1978.

Martin, P.J., A description of the Navy Coastal Ocean Model Version 1.0. NRL Report: NRL/FR/7322-009962, pp. 39, Naval Research Laboratory, Stennis Space Center, MS, 2000.

Oey, L.-Y., and H.-C. Lee, Deep eddy energy and topographic Rossby waves in the Gulf of Mexico, *J. Phys. Oceanogr.*, *32*, 3499-3527, 2002.

Pacanowski, R.C., and A. Gnanadesikan, Transient response in a Z-level ocean model that resolves topography with partial cells, *Monthly Weather Review*, *126*, 3248-3270, 1998.

The reduced grid for the global semi–Lagrangian numerical weather prediction model

Fadeev R. Y.

Institute of Numerical Mathematics, Russian Academy of Sciences,
8 Gubkina ul., 119991 Moscow RUSSIA
email: fadeyev@inasan.rssi.ru

The nodes of the regular latitude–longitude grid become denser as the meridians converge towards the poles. It is well known that the parameterizations of sub–grid processes in the forecast model may work incorrectly on the non–isotropic grid. The method of reduced grid constructing for a spectral model using asymptotic properties of the associated Legendre functions was proposed in [1] and later was modified in [2], [3]. The longitude step of such a grid depends on the latitude. In the present work we describe another approach suitable for semi–Lagrangian finite difference models.

The accuracy of the semi–Lagrangian scheme substantially depends on the interpolation procedure. Thus, the main goal is that to minimize the number of the grid nodes at the fixed upper limit ϵ_Φ:

$$\int_{-\pi/2}^{\pi/2} |\Phi - \Phi_0| \, d\phi_0 \Big/ \int_{-\pi/2}^{\pi/2} \Phi_0 \, d\phi_0 \le \epsilon_\Phi, \tag{1}$$

where $\Phi(\phi_0)$ is the r. m. s. interpolation error of a given symmetric feature $f(\phi_0, \lambda, \phi)$ on the reduced grid and $\Phi_0(\phi_0)$ is calculated on the regular grid. The symmetric feature $f(\phi_0, \lambda, \phi) = \exp(-\mu d^2)$ with center at the point $(0, \phi_0)$ was found to be useful for comparison of different reduced grids. Here d is the distance on the sphere between the center $(0, \phi_0)$ and the point (λ, ϕ); $\mu = -4\ln(10^{-7})/(10.5\Delta\phi)^2$. The radius of the sphere is $a = 1$ and $\Delta\phi$ is the fixed latitude step of the grid.

Equation (1) is solved numerically for each value of ϵ_Φ and we call the grid obtained in such a way as optimal. We found that for the optimal reduced grid the quantity ϵ_Φ depends exponentially on relative reduction of the total number of nodes $n_{\rm rel}$ with respect to the regular grid.

The shallow–water test of Williamson *et al.* [4] which involves the solid–body rotation of a cosine bell around the sphere through the poles demonstrated promising perspectives of our method. The results for the number of latitudes $n_\phi = 125$ and the number of longitudes on the equator $n_\lambda = 200$ are shown in Fig. 1. The quantities Δ_i $(i = 1, 2)$ are normalized r. m. s. errors of the numerical solution calculated on the reduced grid with respect to the exact solution $(i = 1)$ and the numerical solution obtained on the regular grid $(i = 2)$. It should be noted that curves with $n_{\rm rel} = 35.4$ and $n_{\rm rel} = 29.7$ do not represent the optimal grids and the first of them is the reduced grid with constant longitude step on the sphere surface for all latitudes.

The method will be used to construct the reduced grid for the global semi–Lagrangian numerical weather prediction SL–AV model [5]. Latitudinal derivatives in this model

are calculated in the space of longitudinal Fourier coefficients, so the reduced grid can be implemented.

Advantage of our method is that it allows us to take into account various details of the weather prediction model and to apply additional restrictions to the grid. See [6] for comprehensive description of the method. This work was supported by the RFBR grant 04–05–64638.

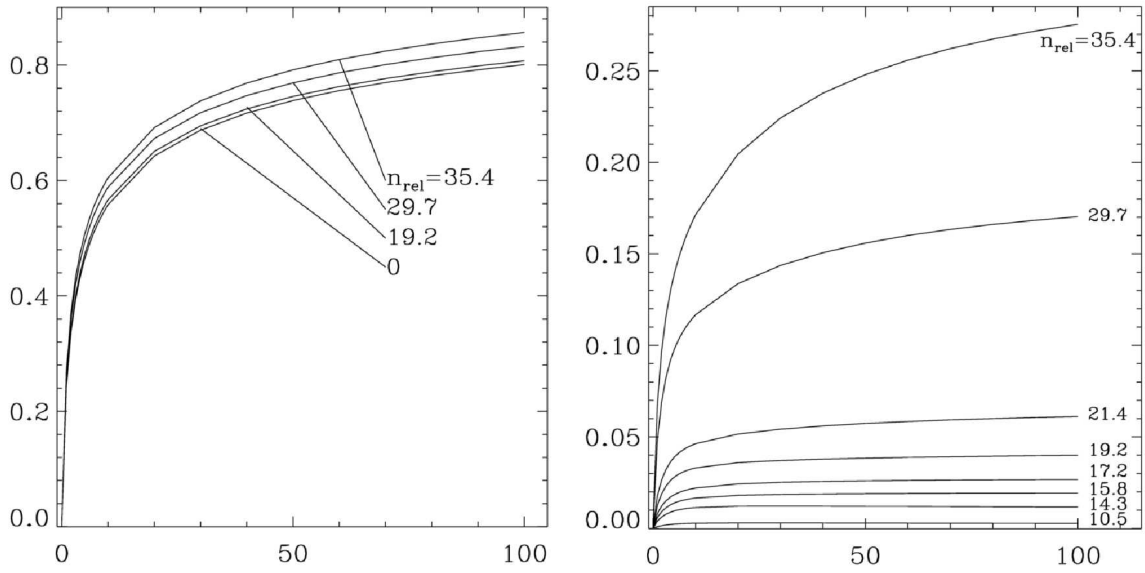

Figure 1: The quantities Δ_1 (left panel) and Δ_2 (right panel) versus the number of complete rotations (255 steps each) on the grids with different relative reduction of the total number of nodes $n_{\rm rel}$ (in per cent).

References

[1] Hortal M., Simmons A. J. Use of reduced Gaussian grids in spectral models. – Mon. Wea. Rev., 1991, vol. 119, pp. 1057–1074.

[2] Naughton M., Courtier P. A pole problem in the reduced Gaussian grid. – Quart. J. Roy. Meteorol. Soc., 1994, vol. 120, pp. 1389–1407.

[3] Williamson D. L., Rosinski J. M. Accuracy of reduced–grid calculations. – Quart. J. Roy. Meteorol. Soc., 2000, vol. 126, pp. 1619–1640.

[4] Williamson D. L., Drake J.B., et al. A standart test set for numerical approximations to the shallow water equations in spherical geometry. – J. Comput. Phys., 1992, vol. 102, pp. 211–224.

[5] Tolstykh M. A. Semi–Lagrangian high resolution model of atmosphere for numerical weather prediction. – Russ. Meteor. and Hydrol., 2001, N 4, pp. 1–9.

[6] Fadeev R. Y. Reduced latitude–longitude grid constructing for the global numerical weather prediction. – submitted to Russ. Meteor. and Hydrol.

[7] Naughton M., Courtier P., Bourke W. Representation errors in various grid and spectral truncations for a symmetric feature on the sphere. – Quart. J. Roy. Meteorol. Soc., 1996, vol. 122, pp. 253–265.

Influence of different vertical and horizontal model resolutions on the simulated hydrological cycle of the GCM ECHAM5

Stefan Hagemann, Klaus Arpe and Erich Roeckner

Max Planck Institute for Meteorology, Bundesstr.53, 20146 Hamburg, Germany, Hagemann@dkrz.de, Roeckner@dkrz.de

A new version of the atmospheric general circulation model (GCM) ECHAM has recently become operational at the Max Planck Institute for Meteorology. For the validation of the hydrological cycle simulated by this new ECHAM5 model (Roeckner et al. 2003), a special focus was set on the influence of different horizontal and vertical resolutions of the ECHAM5 model grid on the quality of the simulated hydrological cycle. The resolutions investigated comprise the spectral horizontal resolutions T42, T63, T106, and T159 as well as two vertical resolutions with 19 (L19) and 31 (L31) vertical levels. The horizontal resolutions correspond to grid sizes of about 2.8°, 1.9°, 1.1° and 0.75° or rather 300 km, 200 km, 110 km and 80 km, respectively. The validation of the simulated hydrological cycle was conducted from the global scale to the regional scale. For the latter, several large catchments are selected which are representative for different climate zones. The validation has shown that increases in vertical and horizontal resolution have a significant impact on the accuracy of the simulated hydrological cycle of ECHAM5. It turned out that an increase in vertical resolution from 19 to 31 levels generally has a larger impact on the simulated hydrological cycle than an increase in horizontal resolution. Despite of the uncertainties of observational estimates over the ocean it seems that the simulated hydrological cycle over the ocean is slightly worsening with an increased resolution. But over land increases in horizontal resolution and especially in vertical resolution have a positive impact on the quality of the simulated hydrological cycle. For some catchments, such as for the Amazon and the Amur catchment with regard to the simulated 2m temperature, only the combined effect of increases in both kinds of resolution lead to a significant improvement. This indicates that the increase of resolution in only one dimension (either vertical or horizontal) may not be sufficient to yield a considerable improvement in the hydrological cycle simulated by a GCM in general. An increase of horizontal resolution from T106 to T159 does not noticeably improve the simulated hydrological cycle. Therefore it is recommended to use T106L31 for future ECHAM5 studies involving the hydrological cycle if computing time is not a limiting factor.

Fig. 1 shows the annual mean biases of the simulated precipitation over selected large catchments that represent various regions from different climates. Over a specific catchment, the bias was calculated from the difference of the simulated precipitation minus GPCP data (Huffman et al. 1997). For most of the catchments, the finer vertical resolution in the L31 simulations leads to a reduction in the precipitation bias. A slight increase of a positive bias is only shown in the Baltic Sea and Arctic Ocean catchment. The effect of an increased horizontal resolution is much smaller than the effect of an increased vertical resolution. A significant bias reduction occurs only in a few catchments (Amur, Baltic Sea, Danube, Nile, Yangtze Kiang), which is most prominent in the Yangtze Kiang catchment. This is clearly related to the much better resolved orography in the very narrow region of the upper catchment part of the Yangtze Kiang river.

The increased vertical resolution causes a reduction of the evaporation bias (not shown) in the majority of catchments. Here, the observed evaporation was calculated from the difference of GPCP precipitation data minus the observed climatological discharge (Dümenil Gates et al. 2000). A relatively large reduction is occurring over the Ganges/Brahmaputra catchment although the bias is still large. This suggests that the increased vertical resolution has a positive effect on the simulation of the Indian monsoon circulation. A significant worsening of the evaporation bias is only seen over the Arctic Ocean catchment. As for precipitation, the effect of an increased horizontal resolution is comparatively small, thereby significantly increasing the positive bias over the Arctic Ocean catchment and slightly reducing the bias over the Congo, Mississippi and Yangtze Kiang catchments.

The combined effect of the precipitation and evaporation biases results in the runoff biases shown in Fig. 2. Here, the runoff bias was calculated by the difference of simulated runoff minus the observed climatological discharge. The increased vertical resolution significantly reduces the runoff biases over almost all catchments. In the Nile catchment, a lot of water is taken from the river for irrigation. As no irrigation information enters the ECHAM5 model this is not simulated. For the Murray, the positive runoff bias is increased with vertical resolution but the Murray catchment covers a very dry area with an annual discharge of only 8 km^3/a (= 258 m^3/s). As there are negative biases in precipitation and evaporation for all model resolutions, even comparatively small deviations (ranging from 2 to 6 km^3/a) of *P-E* (= runoff) from the observed discharge may cause larger runoff bias percentages. The effect of an increased horizontal resolution on the runoff bias is, although mostly smaller than the effect of an

increased vertical resolution, more prominent than for precipitation and evaporation. It generally tends to reduce the runoff bias, especially over the catchments of Amur, Baltic Sea, Danube, Parana and Yangtze Kiang. Only the large runoff bias over the Ganges/Brahmaputra catchment is increased with finer horizontal resolutions.

References

Dümenil Gates, L., S. Hagemann, and C. Golz, Observed historical discharge data from major rivers for climate model validation, Rep. 307, Max-Planck-Inst. für Meteorol,, Hamburg, Germany, 2000.

Huffman, G.J., R.F. Adler, A. Arkin, A. Chang, R. Ferraro, A. Gruber, J. Janowiak, R.J. Joyce, A. McNab, B. Rudolf, U. Schneider und P. Xie, The Global Precipitation Climatology Project (GPCP) combined precipitation data set, *Bull. Amer. Meteor. Soc.*, 78, 5-20, 1997

Roeckner, E., G. Bäuml, L. Bonaventura, R. Brokopf, M. Esch, M. Giorgetta, S. Hagemann, I. Kirchner, L. Kornblueh, E. Manzini, A. Rhodin, U. Schlese, U. Schulzweida, A. Tompkins, The atmospheric general circulation model ECHAM 5. PART I: Model description, Rep. 349, Max-Planck-Inst. für Meteorol., Hamburg, Germany, 2003

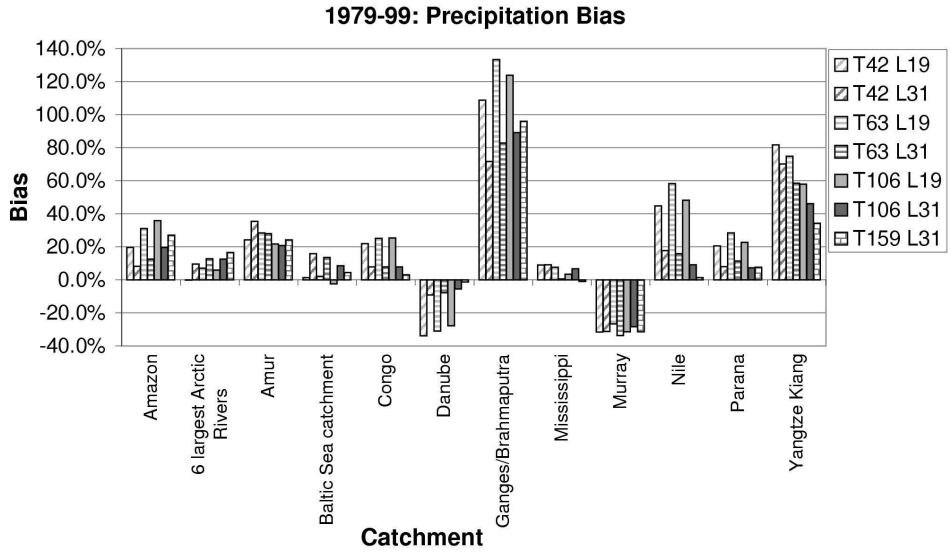

Figure 1 Annual mean bias in simulated precipitation over several catchments. Over a specific catchment, the bias was calculated from the difference of the simulated precipitation minus GPCP data.

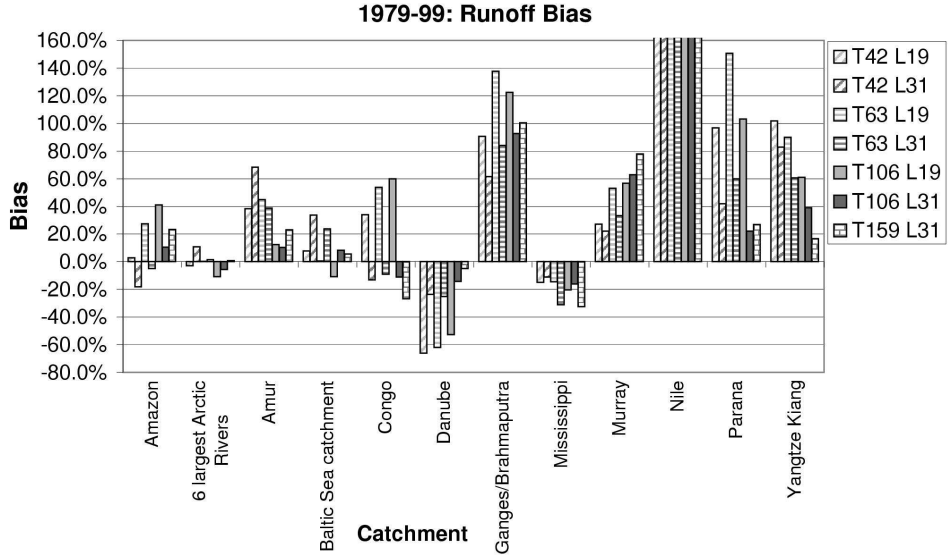

Figure 2 Annual mean bias in simulated runoff over several catchments. The runoff bias was calculated from the difference of the simulated runoff minus the observed climatological discharge.

Fast and Accurate Neural Network Emulation of the NCAR CAM-3 Short Wave Radiation Parameterization: Evaluation of Accuracy of Approximation and Computational Performance

Vladimir M. Krasnopolsky,
Earth System Science Interdisciplinary Center, University of Maryland and SAIC at NCEP/NOAA, USA
Phone: 301-763-8000 x 7262, Fax: 301-763-8545, Email: Vladimir.Krasnopolsky@noaa.gov
Michael S. Fox-Rabinovitz, and Dmitry V. Chalikov
Earth System Science Interdisciplinary Center, University of Maryland, USA

A new approach using neural networks (NN) has been recently developed by the authors for emulating model physics in numerical climate and weather prediction models. This NN approach has been applied first to the long wave radiation (LWR) parameterization in NCAR CAM as the most time consuming part of model physics [*Krasnopolsky et al. 2005*]. The NN emulation of the atmospheric LWR parameterization is fast (about 80 times faster than the original LWR parameterization) and accurate (with practically negligible bias and small rms deviations from the original LWR parameterization). The short wave radiation (SWR) is the second most time consuming part of model physics calculations. In this study, we applied the NN approach to NCAR CAM-3 SWR parameterization. The preliminary evaluation of the NN emulations developed for NCAR CAM-3 SWR parameterization is presented below.

NN approximations of model physics are based on the fact that any parameterization of physics can be considered as a continuous or almost continuous mapping (input vector vs. output vector dependence), and NNs are a generic tool for approximation of such mappings [*Krasnopolsky et al. 2002*]. NN is an analytical approximation that uses a family of functions like:

(1) $$y_q = a_{q0} + \sum_{j=1}^{k} a_{qj} \cdot f(b_{j0} + \sum_{i=1}^{n} b_{ji} \cdot x_i); \quad q = 1,2,\ldots,m$$

where x_i and y_q are components of the input and output vectors respectively, a and b are fitting parameters, and f is a so called activation function (usually it is a hyperbolic tangent), n and m are the numbers of inputs and outputs respectively, and k is the number of neurons in the hidden layer (for more details see appendix in [*Krasnopolsky et al., 2002*]).

The function of the SWR parameterization in atmospheric GCMs is to calculate heat fluxes cased by SWR processes in the atmosphere. In the NCAR CAM SWR parameterization [*J. of Clim. 1998 and the references to W. Collins therein*] used in this study, the calculations of cloudiness are completely separated from the calculations of radiation effects. Due to such a structure convenient for developing NN emulation, we are able to approximate the entire SWR parameterization with only one NN, with cloudiness used just as one of the NN inputs.

Both the original SWR and the NN developed for approximation of the SWR parameterization have 101 inputs (n = 452 in eq. (1)), which include twenty profiles (specific humidity, ozone concentration, relative humidity, fractional cloud cover, in-cloud cloud ice water path, in-cloud cloud liquid water path, liquid effective drop size, ice effective drop size, interface pressure, 12 profiles of aerosol mass mixing ratios) and seven relevant surface characteristics (including cosine of solar zenith angle). This NN has 26 outputs (m = 26 in eq. (1)): a profile of the heating rates (HRs) $\{q_k\}_{k=1,\ldots,26}$. Note that NCAR CAM-3 has 26 vertical levels. The developed NN emulations have one hidden layer with either 50 (NN50) or 100 (NN100) neurons (k = 50 or 100 in eq. (1)) that provide the sufficient accuracy of approximation.

For these initial experiments, a representative data set consisting of about 300,000 input/output combinations has been generated using the two-year NCAR CAM-3 simulation. It was divided into three parts each containing about 100,000 input/output combinations. The first part was used for training, the second one was used for tests (control of over-fitting, control of a NN architecture, etc.), and the third part (the second year) was used for validations only.

Table 1 shows a bulk validation statistics for the accuracy of approximation of our NN emulation for SWR, and also the comparison with the accuracy of the corresponding NN emulation for LWR [*Krasnopolsky et al., 2005*]. NN emulations have been evaluated against the original parameterizations. For calculating the error statistics presented in Table 1, the original parameterization and its NN emulation have been applied to validation data. Two sets of the corresponding HR profiles (for the original parameterization and its NN emulation) have been generated. Bias and RMSE presented in Table 1 have been calculated as the mean and root mean square differences between these two sets of HRs. Mean values and standard deviations (s) of HRs are also presented for a better understanding of relative errors. As mentioned above, our NN emulation for LWR performs about 80 times faster than the original LWR parameterization. Our NN emulation for SWR is approximately two times more complex (has more inputs). As a result it performs about 40 times faster than the original SWR parameterization.

Table 1. Accuracy of Heating Rates (in K/day) calculated using NN Emulations for SWR and LWR for NCAR CAM-3 vs. their Corresponding Original Parameterizations. Mean values and standard deviations (s) of HRs are also presented.

NN	Radiation	Bias	RMSE	Mean HR	σ HR
NN50	SWR	$2. \times 10^{-3}$	0.31	1.47	1.90
	LWR	$1. \times 10^{-3}$	0.38	-1.43	1.76
NN100	SWR	$2. \times 10^{-4}$	0.25	1.47	1.90
	LWR	$4. \times 10^{-4}$	0.33	-1.43	1.76

The obtained results show that the NN emulation of the considered atmospheric SWR parameterization is highly accurate and provides a significantly improved computational efficiency. Using both NN emulations for LWR and SWR will result in a significant, about 40-80 times, acceleration of calculations of the entire radiation block.

The further complete reexamination of computations for all model physics components in NCAR CAM-3 will be done later. This in turn will potentially make a positive practical impact on extensive experimentation with this kind of complex models needed for improving climate change assessments and weather prediction. The developed methodology can be applied to other LWR and LWR schemes used in the variety of models, process studies, and other applications.

The parallel NCAR CAM decadal climate simulations, performed with the original LWR parameterization and its NN emulation, are very close to each [*Krasnopolsky et al., 2005*]. Similar decadal experiments are planned for SWR of NCAR CAM-3.

Acknowledgments. The authors would like to thank Drs. W. Collins, P. Rasch, and J. Tribbia (NCAR) for useful discussions and consultations.

References

Journal of Climate, 1998: v. 11, No. 6 (the special issue).

Krasnopolsky, V.M., M.S. Fox-Rabinovitz, and D.V. Chalikov, 2005: "Fast and Accurate Neural Network Approximation of Long Wave Radiation in a Climate Model", *Monthly Weather Review,* in press,

Krasnopolsky V. M., D. V. Chalikov, and H. L. Tolman, 2002: "A Neural Network Technique to Improve Computational Efficiency of Numerical Oceanic Models", *Ocean Modelling*, v.4, 363-383

Towards an interactive conserving semi-Lagrangian model for chemistry and climate

Ahmed Mahidjiba[(1)], Abdessamad Qaddouri[(2)] and Jean Côté[(2)]
(1) Ouranos/UQÀM, 550 Sherbrooke West Street, 19th floor, Montreal, QC, Canada H3A 1B9
(2) RPN, Meteorological Service of Canada, Dorval, QC, Canada H9P 1J3

1. Introduction

The main purpose of this work is to solve the problem of local conservation for chemistry and climate by using the algorithm developed by Zerroukat & al. (2002). Results of the validation for 2D passive advection were presented in Mahidjiba & Côté (2004). We present validation results of the shallow-water model where this conservative scheme will be implemented. We consider both linear and non-linear problems.

2. Numerical model

The same fully implicit semi-Lagrangian method as in the GEM operational model (Côté et al., 1998, Yeh et al., 2002) is used to discretize the shallow-water equations. That is:

1) Uniform Arakawa staggered C-Grid,
2) 2-time-level iterative semi-Lagrangian method with interpolated in time advecting wind,
3) Iterative non-linear solver for the Helmholtz problem with a direct solver kernel,
4) Iterative treatment of the Coriolis terms by grouping them as with the non-linear terms,
5) Metric terms using the Lagrange multiplier approach of Côté (1988),
6) New trajectory algorithm for staggered limited-area model.

3. Results

Two series of validation experiments where performed: linear and non-linear.

a) Non-rotating linear case

In this linear non-rotating case we linearise the shallow-water equations around a resting basic flow with constant height. In this case the discretised governing equations can be solved analytically and we can compute analytically the expected RMS. We can then compare it to the score obtained be numerical integration. We consider the case of a pure one-dimensional gravity wave (wave-number = 1) in a 1000 km square basin, a resting height of 1 km, a perturbation of 1 m, and Δx = 5000 m. The integration time is one period. The results are shown in Fig. 1 where the black line joins the analytic RMS for a few values of the time step. The numerically computed RMS gives identical value (black dots). We compare also with a Taylor expansion of the exact expression (dotted line). Note that the quartic term is necessary for agreement in the range of time steps considered here, i.e.,

$$RMS_{approximate} = c_0 + c_2\Delta t^2 + c_4\Delta t^4.$$

Δt starts at one tenth of a period and is halved repeatedly.

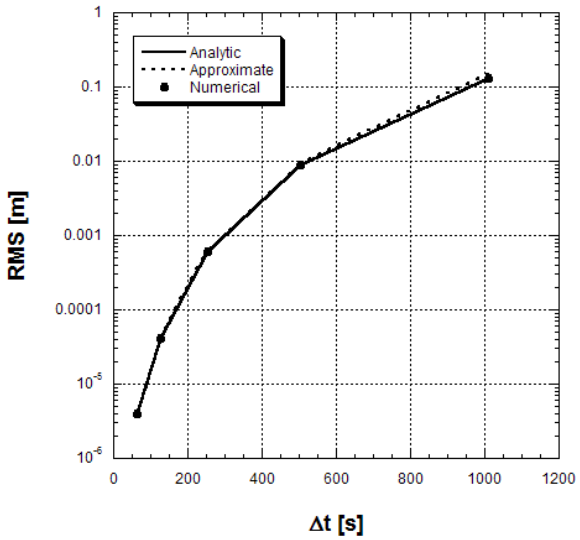

Figure 1: *Numerically computed RMS, analytical expression for RMS and its quartic approximation as functions of time step length.*

b) Rotating non-linear case

The second case is for the full set of non-linear equations with realistic initial conditions and parameters. There is no exact solution in this case and a validation strategy is to compare our results with a carefully controlled experiment published in the literature. Since we run a limited-area model with the same boundary conditions as in Temperton & Staniforth (1986) [TS] and we had their model at our disposal we could repeat their experiment: first with their model and next with our model. The key element is to have

E-Mail: mahidjiba.ahmed.@ouranos.ca

properly balanced initial conditions. In this set of experiments the initialization procedure of TS is used to produce initial conditions to both models. We then run both models from these initial conditions and the same geometry. The scores are produced for the same central window as TS but with all runs performed at uniform resolution. Fig. 2 shows the RMS scores at 48h obtained for the non-linear shallow-water case with realistic initial conditions. We see that the new model is at least equivalent to TS and obtains slightly better results at large time steps. Fig. 3 displays the 48h forecast height field obtained with the new model.

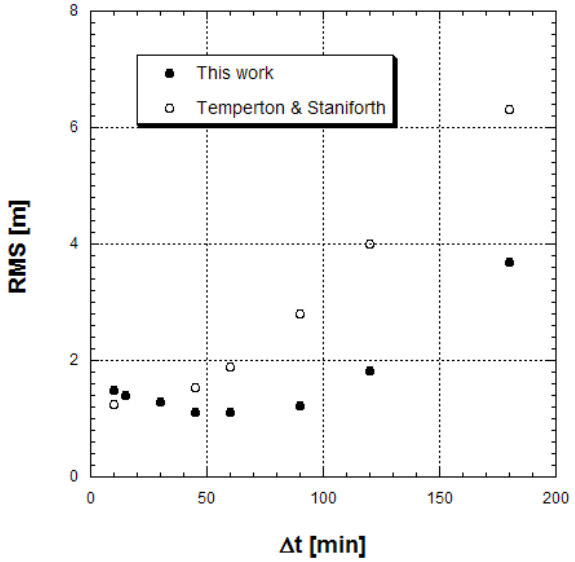

Figure 2: *Total RMS produced by the model of Temperton & Staniforth (1986) and the present model as functions of time step length.*

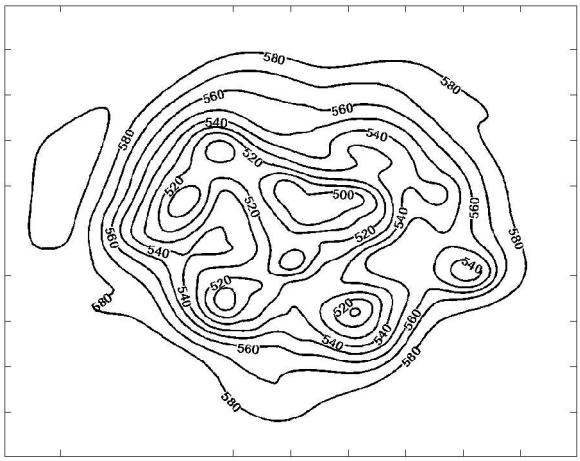

Figure 3: *Geopotential height in dam at 48h with a time step of 1 hour.*

4. Conclusion

As an important preliminary step in implementing the conservative semi-Lagrangian scheme of Zerroukat & al. (2002) interactively in a shallow-water model we presented results of validation experiments performed with the shallow-water model. Since the scheme is nearly the same as that implemented in the operational GEM model it provides a complementary quantitative evaluation.

Acknowledgement: This work is supported by CFCAS through a grant to MAQNet.

References

Côté, J., S. Gravel, A. Méthot, A. Patoine, M. Roch and A. Staniforth, 1998: The operational CMC-MRB global environmental multiscale (GEM) model: Part I - Design considerations and formulation. *Monthly Weather Review*, **126**, pp. 1373-1395.

Staniforth, A. and J. Côté, 1991: Semi-Lagrangian integration schemes for atmosphere models- A review. *Mon. Wea. Rev.*, **119**, 2206-2223.

Zerroukat, M., Wood, N. & Staniforth A., 2002: SLICE: A Semi-Lagrangian Inherently Conserving and Efficient scheme for transport problems, *Q. J. R. Meteorol. Soc.* **128**, 2801-2820.

Mahidjiba, A., & Côté, J., 2004: Conservative Semi-Implicit Semi Lagrangian Method (CSSL) for Transport in Climate and Chemical Models, CAS/JSC Working Group On Numerical Experimentations, **34**. pp. (03)15 – (03)16.

Côté, J., 1988: A Lagrange multiplier approach for the metric terms of semi-Lagrangian models on the sphere, Q. J. R. Meteorol. Soc. **114** pp. 1347-1352.

Temperton C. & Staniforth, A., 1986: An efficient two-time-level semi-Lagrangian semi-implcit integration scheme, Q. J. R. Meteorol. Soc, **113**, pp. 1025-1039.

Yeh, K.-S., J. Côté, S. Gravel, A. Méthot, A. Patoine, M. Roch and A. Staniforth, 2002: The CMC-MRB global environmental multiscale (GEM) model: Part III – Nonhydrostatic formulation. *Monthly Weather Review,* **130**, pp. 339-35.

E-Mail: mahidjiba.ahmed.@ouranos.ca

Analysis of relative dynamics of different cycles with the use of phase portraits

Mokhov I.I.

A.M. Obukhov Institute of Atmospheric Physics RAS, Moscow, Russia

mokhov@ifaran.ru

The method of cycles proposed by Mokhov (1993) (see also Mokhov (1995), Mokhov and Eliseev (1998), Mokhov et al., (2000), Mokhov et al., (2004)) can be extended for the analysis of relative dynamics of different cycles (cross-cycles analysis). It is based on the analysis of phase portraits for given time series $X(t)$. In particular, if there is a statistically significant linear regression of $d^2X(t)/dt^2$ on $X(t)$ with a negative regression coefficient $-\omega^2(t)$, then the process can be fitted by a harmonic oscillator:

$$d^2X/dt^2 + \omega^2 X = 0 \qquad (1)$$

or

$$X(t) = A(t)\sin[\omega(t)t + \varphi(t)] \; . \qquad (2)$$

The amplitude of the process $A(t)$, its frequency $\omega(t)$, and period $P(t) = 2\pi /\omega(t)$, as well as the initial phase $\varphi(t)$, are assumed to change sufficiently slowly with time. Equation (1) is considered at an interval of the length $I_0 \geq P$, such that $|I_0 d\Omega/dt| << \Omega$ and $|I_0 dA_c/dt| << A_c$, where $d\Omega/dt$, Ω, dA_c/dt, and A_c are typical values of $d\omega/dt$, ω, dA/dt, and A respectively (Mokhov and Eliseev, 1998; Mokhov et al., 2004).

The variables dX/dt and d^2X/dt^2 can be determined by taking the second-order finite differences of the original time series $X(t)$. The frequency $\omega(t)$ (and the period $P(t)$) are calculated using the least-squares fitting technique at a moving segment of length I_0. Then, using this same moving segment, the amplitude $A(t)$ and phase $\varphi(t)$ can be determined with the use of the least-squares method and (2). To filter out the higher frequency noise, the raw data can be smoothed taking running means at the window I_s.

The method described above is sensitive to the parameter I_0. On the one hand, I_0 must not be less than the characteristic period of variations in the original data set. On the other hand, I_0 acts as a filter preserving this dominant oscillation modulated by variations with time scales longer than I_0. Thus, it is necessary that

$$I > \tau_P \, , \quad \tau_A >> I_0 \geq 2\pi /\Omega >> I_s$$

or at least

$$I - I_s + \delta t > \tau_P , \quad \tau_A > I_0 \geq 2\pi / \Omega > I_s ,$$

where I is the full length of the time series, δt is its time step, τ_P and τ_A are typical times of the changes with a period P and amplitude A respectively (Mokhov and Eliseev, 1998; Mokhov et al., 2004).

This method can be applied to two variables $X_1(t)$ and $X_2(t)$ separately. Then the phase difference $\Delta\varphi(t) = \varphi_2(t) - \varphi_2(t)$ will characterize the relative dynamics of the corresponding cycles of these two variables. Other characteristics of this cross-cycles analysis can be determined from the corresponding linear regressions at a moving segments of length I_0. In this case the coefficient of linear regression and coefficient of correlation of $X_2(t)$ to $X_1(t)$ (or $X_1(t)$ to $X_2(t)$) characterize the cross-amplitude and coherence, respectively. The first estimates have been obtained with this cross-cycles analysis method for relative dynamics of quasi-decadal and quasi-pentadal cyclicity of North Atlantic and Arctic Oscillations, Pacific/North American teleconnection pattern and El-Nino phenomena.

This work has been partly supported by the Russian Foundation for Basic Research and by the RAS program.

References

1. Mokhov, I.I. (1993) Climate changes: Analyses of global cycles. *Ann. Geophys.,* **12** (Suppl. II), C334.
2. Mokhov, I.I. (1995) Diagnostics of climate system structure and its evolution in the annual cycle and interannual variability. Moscow, IAP RAS, 64 pp. (in Russian)
3. Mokhov, I.I., and A.V. Eliseev (1998) Tendencies of change of QBO characteristics for zonal wind and temperature of equatorial lower stratosphere. *Izvestiya, Atmos. Oceanic Phys.,* **34**, 327-336.
4. Mokhov, I.I., A.V. Eliseev, D. Handorf, V.K. Petoukhov, K. Dethloff, A. Weisheimer, and D.V. Khvorostyanov (2000) North Atlantic Oscillation: Diagnosis and simulation of decadal variability and its long-period evolution. *Izvestiya, Atmos. Ocean Phys.,* **36**, 555-565.
5. Mokhov, I.I., D.V. Khvorostyanov, and A.V. Eliseev (2004) Decadal and longer term changes in El Nino – Southern Oscillation characteristics. *Intern. J. Climatol.,* **24,** 401-414.

Parallel Atmospheric General Circulation Model Code Analysis and Optimization

V.P. Parkhomenko

Computing Centre of the Russia Academy of Sciences

Vavilov Str. 40 Moscow 119967 Russian Federation

E-mail: parhom@ccas.ru

Computing Centre (CC) atmospheric general circulation model (AGCM) uses uniform 72 on longitude and 46 on a latitude horizontal grid for single processor computer. Program was modified for high performance cluster. An analysis is presented of the primary factors influencing the performance of a parallel implementation of AGCM on distributed-memory, cluster computer system. Several modifications to the original parallel AGCM code aimed at improving its numerical efficiency, load-balance code performance are discussed. The impact of these optimization strategies on the performance on MVS 1000M parallel computer is presented and analyzed. There are two major components of the AGCM model code: Dynamics, which computes the evolution of the fluid flow governed by the primitive equations by means of finite-differences, and Physics, which computes the effect of processes not resolved by the model's grid (such as convection on cloud scales) on processes that are resolved by the grid. The AGCM Dynamics itself consists of two main components: a spectral filtering part and the finite difference calculations. The filtering operation is needed at each time step in regions close to the poles to ensure the effective grid size there satisfies the stability requirement for explicit time-difference schemes when a fixed time step is used throughout the entire spherical finite-difference grid.

It is found that implementation of a load-balanced Fourier algorithm results in a reduction in overall execution time of approximately 40% compared to the original algorithm. Preliminary results of the application of a load-balancing scheme for the Physics part of the AGCM code suggest additional reductions in execution time of 15% can be achieved.

A two-dimensional grid partition in the horizontal plane is used in the parallel implementation of the AGCM model. Each subdomain in such a grid is a rectangular region which contains all grid points in the vertical direction. Timing measurements on the main components of the original parallel AGCM code, using the 4 x 5 x 9 degrees resolution are shown on Table.

Table. Execution times of major components in the AGCM code

Number of processors	Dynamics, %	Physics, %	Fourier in Dynamics, %
1	63	33	10
8	67	30	18
16	70	27	20

Comparing the two modules in the main body, we can see the Dynamics part is dominant in cost especially on large numbers of nodes. Furthermore, our timing analysis on the Dynamics part indicates that the spectral filtering is a very costly component.

To solve the load-balance problem in filtering, we need to redistribute the data rows to be filtered along the latitudinal direction. In the AGCM code, the spectral filtering is

performed at each time step before the finite-difference procedures are called. If it could be assumed that exactly half of the data rows in one hemisphere are to be filtered, the implementation of data redistribution for load balancing would be a relatively simple task.

The Physics component of the AGCM code consists of a large amount of local computations with no interprocessor communication required with the two-dimensional partition of the grid. The amount of computation required at each grid point is determined by several factors, including whether it is day or night, the cloud distribution, and the amount of cumulus convection determined by the conditional stability of the atmosphere. Adding to the difficulty of physics load-balancing is the unpredictability of the cloud distribution and the distribution of cumulus convection, which implies an estimation of computation load in each processor is required before any efficient load-balancing scheme can proceed.

The computation load for each processor needs to be computed or estimated by some means. The approach that we decided to adopt requires only pair wise interprocessor communications for data movement and a small amount of bookkeeping. The scheme begins with an evaluation of the local load in each processor whether it is day or night. The data load is sorted , and a pair-wise data exchange between processors is initiated for balancing the load. We would expect even better scaling be achieved for the parallel filtering as well as for the overall AGCM code for higher horizontal and vertical resolution versions.

References

Wehner, M.F., A.A. Mirin, P.O. Eltgroth, WP. Dannevik, C.R. Mechoso, J. Farrara, J.A. Spahr, Performance of a Distributed Memory Finite-Difference Atmospheric General Circulation Model, Parallel Computing 21, 1655-1675, 1995.

Lou, J. Z., J. D. Farrara, Performance Analysis and Optimization on a Parallel Atmospheric General Circulation Model Code, ISSN 1063-7133/97, 1997.

NUMERICAL SOLUTION OF THE REACTION–ADVECTION–DIFFUSION EQUATION ON THE SPHERE

Janusz A. Pudykiewicz, MSC, RPN, e-mail: Janusz.Pudykiewicz@ec.gc.ca

In order to provide an alternative to semi–Lagrangian techniques for the solution of the reaction–advection–diffusion equation, a simple yet accurate Eulerian algorithm build upon the principle of finite volumes has been developed. The set of the considered equations has the following form:

$$\frac{\partial \varphi^k}{\partial t} = -\nabla \mathbf{u}\varphi^k + \nabla \mathbf{K}\nabla\varphi^k + F_{\rm c}^k(\varphi^1,\ldots,\varphi^{N_{\rm s}}), \tag{1}$$

where φ^k is the $k^{\rm th}$ scalar field; $k = 1,\ldots,N_{\rm s}$, $N_{\rm s}$ is number of scalar fields, $\mathbf{u}$ is the three–dimensional velocity field, $\mathbf{K}$ is the diffusion tensor, and $F_{\rm c}^k$ are the functions describing the interactions between scalar fields. In a most general case, $F_{\rm c}^k$ can be written as $\alpha_{klm}\varphi^l\varphi^m + \beta_{kl}\varphi^l$, where α_{klm} and β_{kl} are the kinetic coefficients. The approach adopted here exploits the concept of semidiscretization (Leveque, 2002; page 191); first, the convective and diffusive fluxes in (1) are approximated and then, the resulting set of the Ordinary Differential Equations (ODEs) is solved using the appropriate time stepping algorithm. This methodology has been selected because of both its flexibility with respect to the mesh selection and its inherent ability to represent subgrid-scale processes and discontinuities in the solution.

The method is initially applied on a geodesic icosahedral grid composed of triangles with vertices located on the spherical surface (Fig. 1). The control volume Ω_i associated with the $i^{\rm th}$ node is created by a two step procedure. In the first step, the centers of the triangles and the mid-points of the edges are projected on the surface of the sphere. In the second step, Ω_i is defined as a polygon with the vertices located at the projected points (Fig. 2). Equation (1) is then integrated over Ω_i and from the Green theorem,

$$\frac{d\phi_i^k}{dt} = -\frac{1}{S(\Omega_i)}\int\limits_{\partial\Omega_i}(\mathbf{u}\varphi^k - \mathbf{K}\nabla\varphi^k)\,\mathbf{n}\,dl + \frac{1}{S(\Omega_i)}\int\limits_{\Omega_i} F_{\rm c}^k d\mathbf{r}, \tag{2}$$

where $\phi_i^k = \int_{\Omega_i}\varphi^k(\mathbf{r},t)d\mathbf{r}/S(\Omega_i)$, $i \in [1,N_{\rm p}]$, $N_{\rm p}$ is the number of nodes, $k \in [1,N_{\rm s}]$, and $S(\Omega_i)$ is the surface of Ω_i. After discretizing of the integral terms, equation (2) can be written in a compact vector form as

$$\frac{d\boldsymbol{\phi}}{dt} = -(\mathbf{I}_{N_{\rm s}} \otimes \mathbf{A}_{\mathcal{D}})\boldsymbol{\phi} + \mathbf{F}(\boldsymbol{\phi}), \tag{3}$$

where $\mathbf{A}_{\mathcal{D}}$ is the sparse matrix representing the advection–diffusion operator, $\mathbf{I}_{N_{\rm s}}$ is the $N_{\rm s}\times N_{\rm s}$ diagonal matrix, $\otimes$ denotes the Kronecker product, $\mathbf{F}(\boldsymbol{\phi})$ is the vector of forcings, and $\boldsymbol{\phi}$ is the vector of the finite volume averages of the scalar fields

$$\boldsymbol{\phi} = [\phi_1^1,\phi_2^1,\ldots,\phi_{N_{\rm p}}^1,\phi_1^2,\phi_2^2,\ldots,\phi_{N_{\rm p}}^2,\ldots,\phi_1^{N_{\rm s}},\phi_2^{N_{\rm s}},\ldots,\phi_{N_{\rm p}}^{N_{\rm s}}]^{\rm T}.$$

Depending on the stiffness of the system, the time integration of (3) is performed either with the $4^{\rm th}$ order Runge-Kutta scheme or with the Rosenbrock solver . The monotonicity of the scheme is achieved with the explicit local adaptive dissipation proposed by Shchepetkin and McWilliams (1998). The performance of the advection–diffusion solver is assessed using the suite of standard tests based on the solid body rotation of a cosine hill and a cylinder as well as the multiscale signal as suggested by Smolarkiewicz and Grabowski (1989); see Fig. 3 for sample results. The main conclusion from these tests is that the presented method offers mass conservation, quasi monotonicity and good accuracy. Also, the algorithm is stable for the advection with Courant numbers of the order of 2.5, similarly as in the advection tests on structured meshes reported by Vreudeghill (1993).

In order to fully evaluate the method, the reaction–diffusion system on the sphere was also considered. The comparison of the numerical results to the analytical solution presented by Turing (1952) shows that the method is quite accurate with the maximum error not exceeding 0.01%. The solver was also applied for the integration of the nonlinear chemical kinetics system known as a Brusselator (Prigogine and Lefever, 1968).

The main intended application of the reaction-advection-diffusion solver is the simulation of the chemical constituents in the Earth atmosphere. The scheme described herein can also be easily applied on arbitrary differentiable manifolds and, therefore, it is a good candidate for a simulation of tracer transport for both small and large scale flows. The future work will explore numerical solutions of the shallow water equations on the sphere as well as reactive flows at small scales.

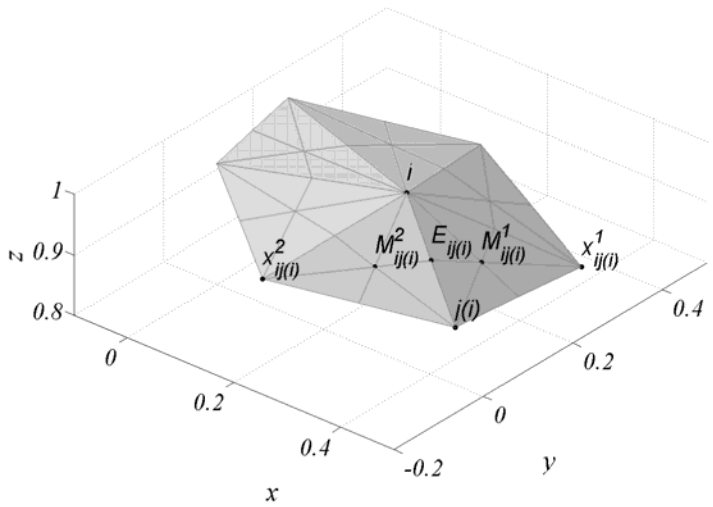

Fig.1 Triangles used in the definition of the finite volumes on the sphere; (i - is the i^{th} node, $j(i)$ - is the node defining one of the incident edges, $E_{ij(i)}$ – is the mid-point of the $(i,j(i))$ edge, $M^l_{i(j(i))}$ – is the mass center of the triangle defined by points: i, $j(i)$, and $x^l_{ij(i)}$ $(l=1,2)$.

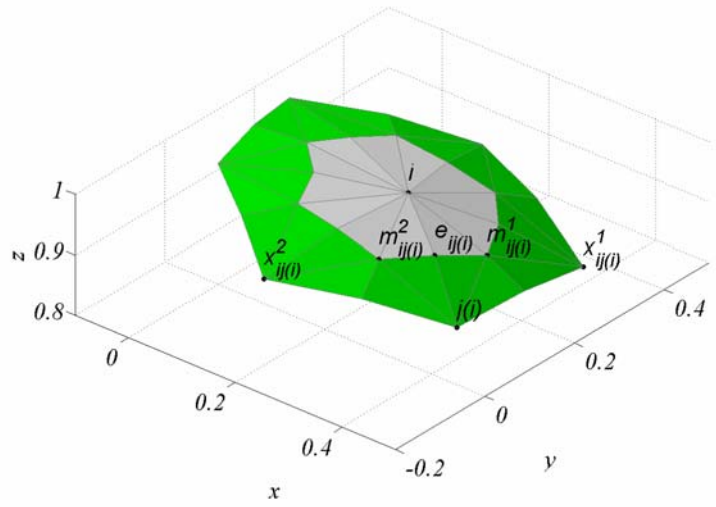

Fig. 2 Finite volume Ω_i (gray polygon); $e_{ij(i)}$, $m^l_{ij(i)}$ denote projected points $E_{ij(i)}$ and $M^l_{ij(i)}$ respectively $(l=1,2)$.

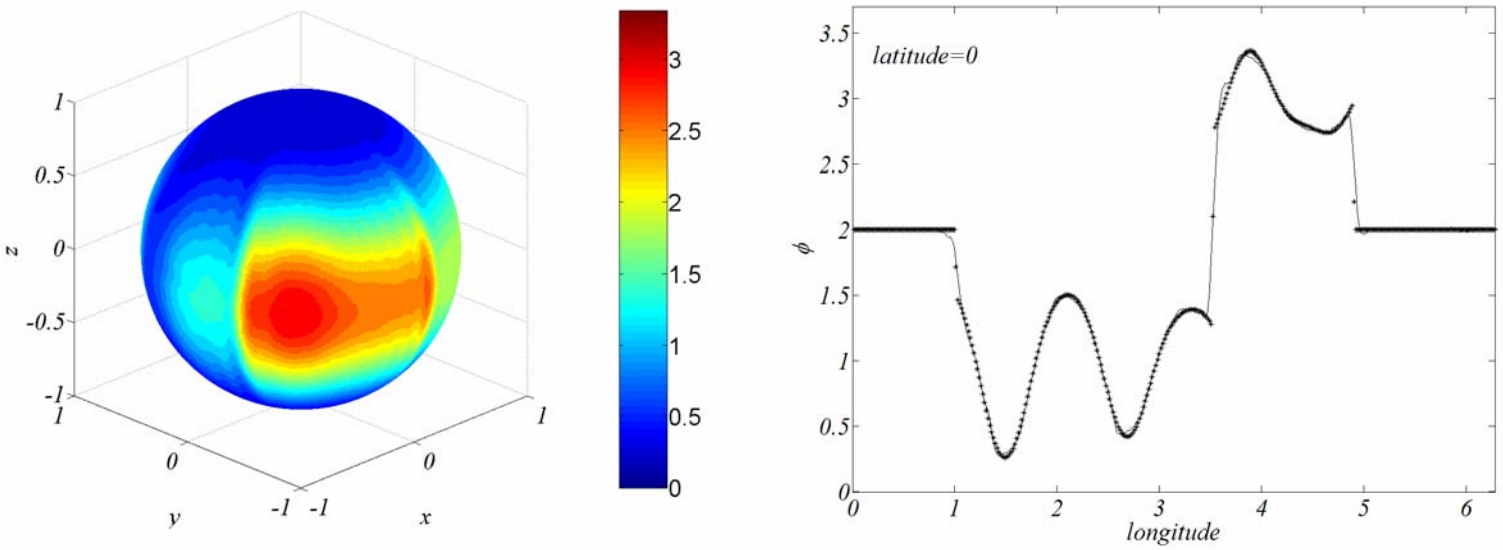

Fig. 3 The solid body rotation of the multiscale signal after one revolution around the equator. The left panel shows results plotted directly on the surface of the sphere whereas the right panel both the analytical solution (dashed line) and the numerical solution (line marked by stars). The initial condition for the test is described by the following function

$$\phi(\theta,\lambda)=\cos^4(\theta)\,(f_1(\lambda)+f_2(\lambda)+2)\left(1+0.3\sin\left(\frac{50}{9}\lambda\right)\right)\left(1+0.4\sin\left(\frac{50}{10}\lambda\right)\right)$$

$f_1(\lambda)=-1$ for $\lambda\in D_1=[8\pi/25,\,28\pi/25]$, $f_1(\lambda)=0$ for $\lambda\in[0,2\pi]-D_1$

$f_2(\lambda)=1$ for $\lambda\in D_2=[28\pi/25,\,39\pi/25]$, $f_2(\lambda)=0$ for $\lambda\in[0,2\pi]-D_2$

(θ is the latitude and λ is the longitude)

References

Leveque R. J., 2002: Finite Volume Methods for Hyperbolic Problems. Cambridge University Press, Cambridge.

Prigogine I. and R. Lefever, 1968: Symmetry-Breaking Instabilities in Dissipative Systems., J. Chem. Phys., 48, 1695-1700.

Shchepetkin A. and J. C. McWilliams, 1998: Quasi-Monotone Advection Schemes Based on Explicit Locally Adaptive Dissipation. Mon. Wea. Rev., 126, 1541-1580.

Smolarkiewicz P. K. and W. W. Grabowski, 1990: The Multidimensional Positive Denite Advection Transport Algorithm: Nonoscillatory Option. J. Comp. Phys., 86, 355-375

Turing A. M., 1952: The Chemical Basis of Morphogenesis. Phil. Trans. of the Roy. Soc. of London, Series B, 237, 3772.

Vreugdenhill C. B., 1993: Linear Central-Difference Methods. Notes on Numerical Fluid Mechanics; Vol 45, Numerical Methods for Advection-Diffusion Problems, editted by Vreugdenhill C. B. and B. Koren, Braunschweig, Viesbaden, 2754.

Optimized Schwarz methods with an overset grid system for the Shallow-Water Equations

Abdessamad Qaddouri[1], Lahcen Laayouni[2], Jean Côté[1,4] and Martin Gander[2,3]
1-Recherche en prévision numérique, Meteorological Service of Canada, Dorval, QC, H9P 1J3 Canada
2-Department of Mathematics and Statistics, McGill University, Montreal, Canada, QC, H3A 2K6 Canada
3-Section de Mathématiques, Université de Genève, Genève, CH-1211 Switzerland
4-Ouranos/UQÀM, 19th floor, 550 Sherbrooke West, Montreal, QC, H3A 1B9 Canada

Abstract. The overset grid system nicknamed "Yin-Yang" grid (Kageyama & Sato, 2004) is singularity free and has quasi-uniform grid spacing. It is composed of two identical latitude/longitude orthogonal grid panels that are combined to cover the sphere with partial overlap on their boundaries. The system of Shallow-Water equations (SWEs) is a hyperbolic system at the core of many models of the atmosphere. In this paper, the SWEs are solved on the Yin-Yang grid by using a semi-implicit and semi-Lagrangian discretization on a staggered mesh. The scalar elliptic equation is solved using a Schwarz-type domain decomposition method, known as the optimized Schwarz method, which gives better performance than the classical Schwarz method by using specific Robin or higher order interface conditions.

1. Introduction

The same fully implicit semi-Lagrangian method as in the GEM operational model is used to discretize the shallow-water equations as in Mahidjiba et al. (2005) except for the use of spherical trajectories: uniform Arakawa staggered C-Grid, 2-time-level iterative semi-Lagrangian method with interpolated in time advecting wind, iterative non-linear solver for the Helmholtz problem, iterative treatment of the Coriolis terms by grouping them with the non-linear terms, metric terms using the Lagrange multiplier approach of Côté (1988). This discretization is implemented independently on each quasi-uniform lat/long part grid. The trajectories are computed for each grid panel in three-dimensional Cartesian geometry with the restriction that the trajectories are confined on the surface of the sphere. The value at an upstream point is determined by the cubic Lagrange interpolation either in Yin (if this point is in Yin) or Yang grid panel. The semi-implicit treatment of the gravity terms in the SWEs gives rise to a 2D elliptic boundary value problem that must be solved at each time step. We use in this work the domain decomposition method, where the solution of the global elliptic problem is obtained by iteratively solving the corresponding two sub-problems separately on the Yin and Yang grids, and updating the values at the interfaces boundaries. The classical alternating Schwarz method consists in using each sub-problem's updated solution as boundary condition to the other one. Because the two grids do not match, the update is done with a cubic Lagrange interpolation and this corresponds to Dirichlet interface conditions. The use of specific Robin or higher order interface conditions improves the convergence of the elliptic solver.

2. Preliminary results

In the first experiment, a cosine bell is advected once around the sphere. This simulation is carried out with a resolution of 150×50 on the Yin grid and 150×50 on the Yang grid, this is equivalent to a global horizontal resolution of about 200 km. A time step of two hours is used, and it requires 144 time steps (288 hrs) to rotate the cosine hill one full revolution around Earth. Fig. 1 shows that there is no distortion in the shape of the hill at the end of the simulation. The bell structure is maintained in the Yin-Yang grid system even when the bell passes trough the overlap region. The time evolution of the normalized maximum difference is presented in Fig. 2 and as can be seen the trend and values of the norm are comparable to those in Jacob-Chien et al. (1995), and the maximum difference after 12 days is small and is about 2%.

For the next experiment we compare the convergence of the iterative elliptic solver for Dirichlet and Robin interface boundaries conditions respectively. Fig. 3 shows that the convergence is improved when Robin interface conditions are used. In this experiment the Helmholtz coefficient is equal to one (hard case) and we take the coefficient in the Robin condition also equal to one. The optimal value of this later coefficient can be found numerically and is expected to further improve the convergence.

E-Mail : abdessamad.qaddouri@ec.gc.ca

3. Conclusion

In this work we show that numerical algorithms already validated for a global latitude/longitude grid can be implemented, with minor changes, for the Yin-Yang grid system while preserving the same temporal and spatial errors. In the near future we will implement optimal Robin and second order interface conditions in order to improve the convergence of the elliptic solver, and the remaining shallow water test cases will be conducted. A parallelization strategy for this model will also be examined.

Acknowledgement. We acknowledge the support of CFCAS trough a grant to the QPF network. This research was partly supported by the Office of Science (BER), U. S. Department of Energy, Grant No. DE-FG02-01ER6319.

References

Jacob-Chien, R., Hack, J.J. & Williamson, D.L., 1995: Spectral transform solutions to shallow-water test set. J. of Comp. Phys. **119**, 164-187

Kageyama, A. & Sato, T., 2004: *The "Yin-Yang Grid": An Overset Grid in Spherical Geometry*, Geochem. Geophys. Geosyst., Q09005, doi:10.1029/2004GC000734; physics/0403123

Mahidjiba, A., Qaddouri, A. & Côté, J., 2005: Towards an interactive conserving semi-Lagrangian model for chemistry and climate. Research Activities in Atmospheric and Oceanic Modelling, J. Côté (ed), **35** (this volume).

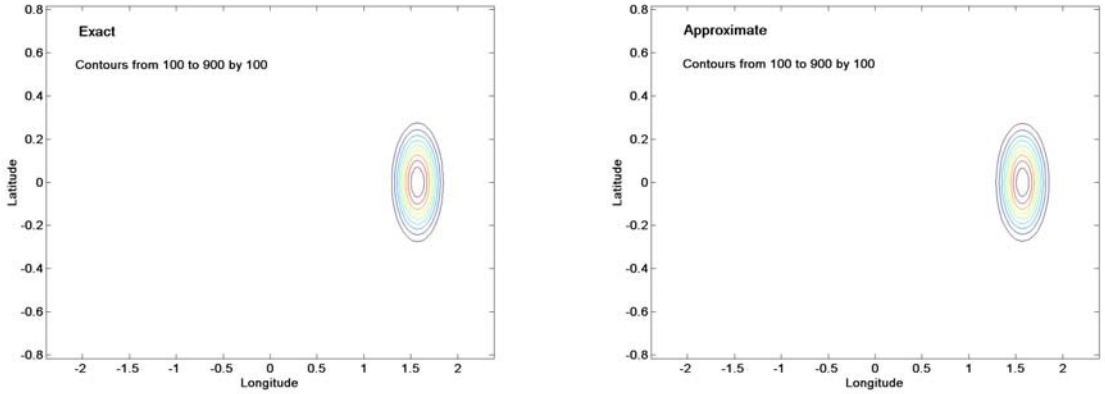

Figure 1: *Exact and approximate scalar field after one revolution around the sphere*

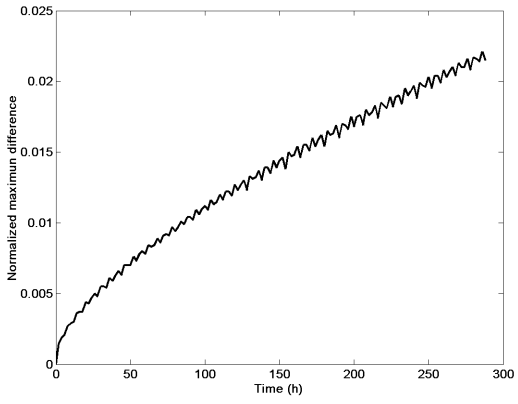

Figure 2: *Evolution of the normalized maximum difference during one revolution*

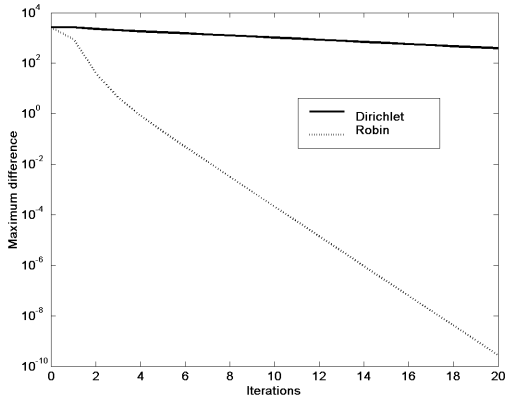

Figure 3: *Comparison of Dirichlet and Robin interface conditions on the convergence of the elliptic solver*

A two-time-level vertically-conservative semi-Lagrangian semi-implicit double Fourier series AGCM

Hiromasa Yoshimura
Climate Department, Meteorological Research Institute, Japan Meteorological Agency
E-mail: hyoshimu@mri-jma.go.jp
Takayuki Matsumura
Numerical Prediction Division, Japan Meteorological Agency

1. Introduction

We developed a three-time-level vertically conservative semi-Lagrangian scheme (Yoshimura and Matsumura 2003), in which computation of the advection terms is split into the horizontal and the vertical directions and the flux in the vertical direction is evaluated with a conservative semi-Lagrangian scheme.

We have also developed a two-time-level version of the vertically conservative semi-Lagrangian scheme which is about twice more efficient than a three-time-level scheme. We adopt new methods shown below to improve stability of the two-time-level scheme.

We have also succeeded in developing a spectral AGCM using double Fourier series instead of conventional spherical harmonics as basis functions. The double Fourier series model is as accurate as and more efficient than the spherical harmonics model.

2. Improvement of stability of the two-time-level vertically conservative semi-Lagrangian scheme

We improve stability of the two-time-level scheme by adopting SETTLS (Hortal 2002) for nonlinear terms, second-order decentering (Temperton et al. 2001) and the methods shown below to avoid extrapolation in time, a source of instability.

○ The wind integrated in a semi-Lagrangian scheme instead of the wind extrapolated in time is used for horizontal trajectory calculations (Yoshimura 2002). This scheme is similar to but more accurate than the scheme of Gospodinov et al. (2001).

○ The potential temperature instead of the temperature is advected horizontally to avoid calculation and time extrapolation of the heating term related to the horizontal advection. On the other hand, the heating term related to the horizontal divergence is calculated in a conventional finite difference method.

3. Double Fourier series model

T (Temperature), $\ln p_s$, $U = u\cos\theta$ and $V = v\cos\theta$ (where u and v are the component of the horizontal wind and θ is latitude) are expanded from gridpoint space to spectral space with the same basis functions of double Fourier series as in Cheong (2000a, 2000b). For example, T is expanded as

$$T(\lambda,\phi) = \sum_{m=-M}^{M} T_m(\phi) e^{im\lambda}$$

$$T_m(\phi) = \begin{cases} \sum_{n=0}^{N} T_{nm}\cos n\phi & \text{for } m = 0 \\ \sum_{n=1}^{N} T_{nm}\sin n\phi & \text{for odd } m \\ \sum_{n=1}^{N'} T_{nm}\sin\phi\sin n\phi & \text{for even } m(\neq 0), \end{cases}$$

where $\phi = \theta + \pi/2$, θ is latitude and λ is longitude.

The zonal Fourier filter (Cheong 2000a) is used to filter out the high zonal wavenumber components near the poles. The biharmonic spectral filter (Cheong et al. 2002), that is, the 4th-order horizontal diffusion (∇^4) is also used. The same coefficient of the diffusion as in the spherical harmonics model is enough for stable integrations because the use of the semi-Lagrangian scheme improves stability of the double Fourier series model (Yoshimura 2002).

The semi-implicit calculation of the double Fourier series AGCM is efficient. The Helmholtz equation related to the semi-implicit calculation can be easily solved through the diagonalization in the vertical direction (Yessad and Benard 1996) and the inversion of the tridiagonal matrix in the horizontal direction (Cheong 2000b).

4. Prediction experiment

We performed a prediction experiment from 00 UTC 9 July 2002 at TL319L40 resolution. We used three models (a), (b) and (c) shown in Table 1. Fig.1 shows 2-day forecasts of sea level pressure and Fig 2 shows 2-day precipitation forecasts. The results of (a), (b) and (c) are in good agreement. This indicates that these three models are of the same accuracy.

Table 1 also shows the execution time of three-day integrations with 1 CPU of NEC SX6. The execution time of (b) is about half of (a) because the time step of the two-time-level model can be twice of that of the three-time-level model. The execution time of (c) is shorter than (b). This is because the Legendre transform (whose operational count is $O(N^3)$ with N the meridional maximum wavenumber) used in the spherical harmonics model is replaced to

the cost-effective Fourier transform (whose operational count is $O(N^2 \log N)$) in the double Fourier series model. The better efficiency of the double Fourier series model against the spherical harmonics model is expected to become more dominant at higher resolutions.

Table 1. The models used in the experiment and the execution time of 3-day integrations

	Integration scheme	Basis function	Resolution	Time step	Execution time
(a)	Three-time-level	Spherical harmonics	TL319L40	10 min.	131 min.
(b)	Two-time-level	Spherical harmonics	TL319L40	20 min.	74 min.
(c)	Two-time-level	Double Fourier series	ML319L40	20 min.	67 min.

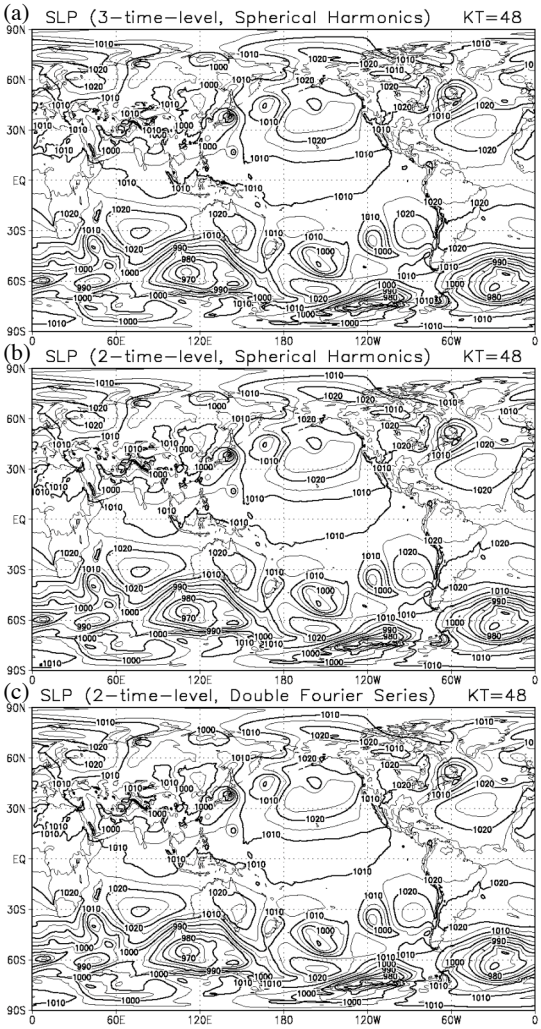

Fig.1. 2-day forecasts of sea level pressure.

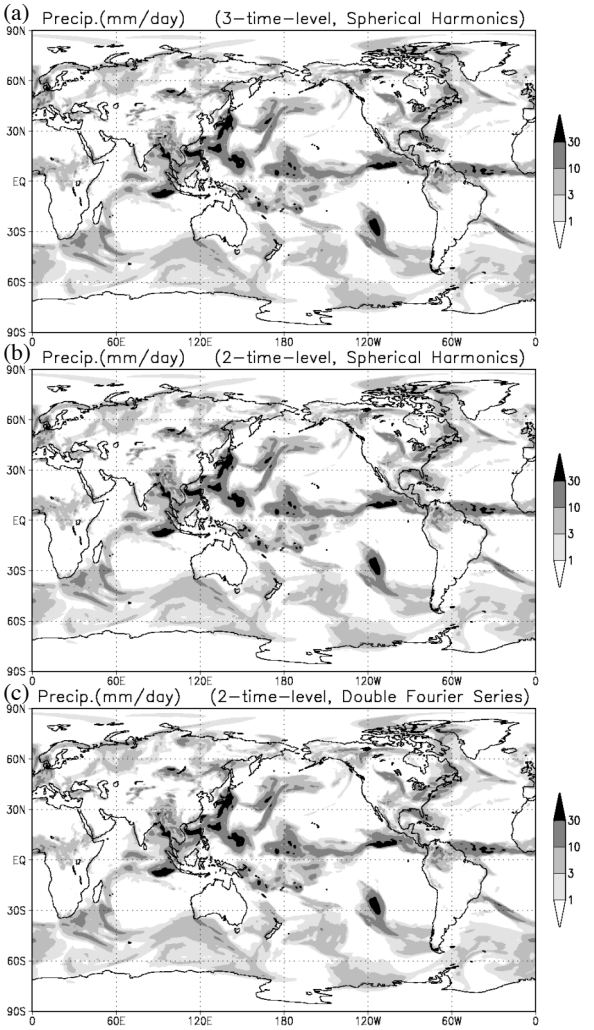

Fig. 2. 2-day precipitation forecasts.

Reference

Cheong, H.-B., 2000a: Double Fourier Series on a Sphere: Applicatons to Elliptic and Vorticity Equations. *J. Comput. Phy.*, **157**, 327-349.,

Cheong, H.-B., 2000b: Application of Double Fourier Series to the Shallow-Water Equations on the Sphere. *J. Comput. Phy.*, **165**, 261-287.

Cheong, H.-B., In-Hyuk Kwon, Tae-Young Goo and Myeong-Joo Lee, 2002: High-Order Harmonic Spectral Filter with the Double Fourier Series on a Sphere. *J. Comput. Phy.*, **177**, 313-335.

Gospodinov, I., V. Spiridonov and J.-F. Geleyn, 2001: Second-order accuracy of two-time-level semi-Lagrangian schemes. *Q. J. R. Meteorol. Soc.*, **127**, 1017-1033.

Hortal, M., 2002: The development and testing of a new two-time-level semi-Lagrangian scheme (SETTLS) in the ECMWF forecast model. *Q. J. R. Meteorol. Soc.*, **128**, 1671-1687.

Temperton, C., M. Hortal and A. Simmons, 2001: A two-time-level semi-Lagrangian global spectral model. *Q. J. R. Meteorol. Soc.*, **127**, 111-127.

Yessad, K. and P. Benard, 1996: Introduction of a local mapping factor in the spectral part of the Meteo-France global variable mesh numerical forecast model. *Q. J. R. Meteorol. Soc.*, **122**, 1701-1709.

Yoshimura, H. 2002: Development of a Semi-Implicit Semi-Lagrangian Global Model using Double Fourier Series. The 4th International Workshop on Next Generation Climate Models for Advanced High Performance Computing Facilities.

Yoshimura, H. and T. Matsumura 2003: A Semi-Lagrangian Scheme Conservative in the Vertical Direction. CAS/JSC WGNE Research Activities in Atmospheric and Ocean Modeling, **33**, 3.19-3.20.

Semi-Lagrangian advection and conservation[i]

Mohamed Zerroukat, Nigel Wood and Andrew Staniforth, Met Office, UK.
mohamed.zerroukat@metoffice.gov.uk

Semi-Lagrangian (SL) schemes are widely used for the advection component of many modern operational atmospheric models due to their increased efficiency and stability compared to Eulerian schemes. However, a common disadvantage of interpolating SL schemes is the lack of mass and tracer conservation. Though mass conservation may not be critical for short period NWP simulations, it is very important for long period simulations such as those of climate studies. Over a long simulation period, the total mass can drift significantly if no correction is applied. Hence, SL schemes which are inherently mass conserving are desirable. The challenge is to not only achieve inherent conservation, but to do so whilst minimising the additional cost over that of a traditional interpolating SL scheme. This motivated the development of Zerroukat et al. (2002)'s Semi-Lagrangian Inherently Conserving and Efficient (SLICE) algorithm.

There are two ingredients. The first is to rewrite the Eulerian flux form

$$\frac{\partial \rho}{\partial t} + \nabla \cdot (\rho \mathbf{u}) = 0,$$

where ρ is a scalar field transported by velocity $\mathbf{u}$, in a finite-volume Lagrangian form

$$\frac{D}{Dt} \int_{\partial V} \rho dV = 0 \Rightarrow M_a^{n+1} = M_d^n.$$

Here ∂V is a fluid parcel or Lagrangian control volume, M_a^{n+1} is its mass at time $(n+1)\,\Delta t$ centred on the arrival location $\mathbf{x}_a$, and M_d^n its mass at time $n\Delta t$ centred on the departure location $\mathbf{x}_d$. The second is to adapt Purser & Leslie (1991)'s cascade remapping strategy to very efficiently decompose a two-dimensional remapping problem (from Eulerian control volumes to Lagrangian ones, or vice-versa) into a number of much-simpler one-dimensional remapping problems - see Zerroukat et al. (2002) for details. An important property of cascade remapping is that it preserves characteristics of the flow, thus minimising splitting errors. Overall, it is found that in addition to exactly conserving mass, the SLICE algorithm is also competitive with standard non-conserving semi-Lagrangian schemes from the viewpoints of both computational efficiency and accuracy.

Zerroukat et al. (2002)'s algorithm in planar geometry has been extended to spherical geometry in Zerroukat et al. (2004) with no restriction on Courant numbers. A simple further extension of the SLICE algorithm is described in Zerroukat et al. (2005) which allows monotonicity (and positive-definiteness) to be efficiently imposed in both planar and spherical geometry. This extension operates by first identifying where monotonicity is violated (the detection stage), and by then locally reducing the order of the piecewise polynomial used in the remapping algorithm until monotonicity is regained (the reduction stage). A global minimum and/or a global maximum can similarly be imposed and positive-definiteness is achieved by setting the global minimum to be zero. The resulting monotonicity scheme has been applied to various test cases. Illustrative comparative results for the challenging, non-smooth, deformational problem on the sphere are displayed in Fig. 1.

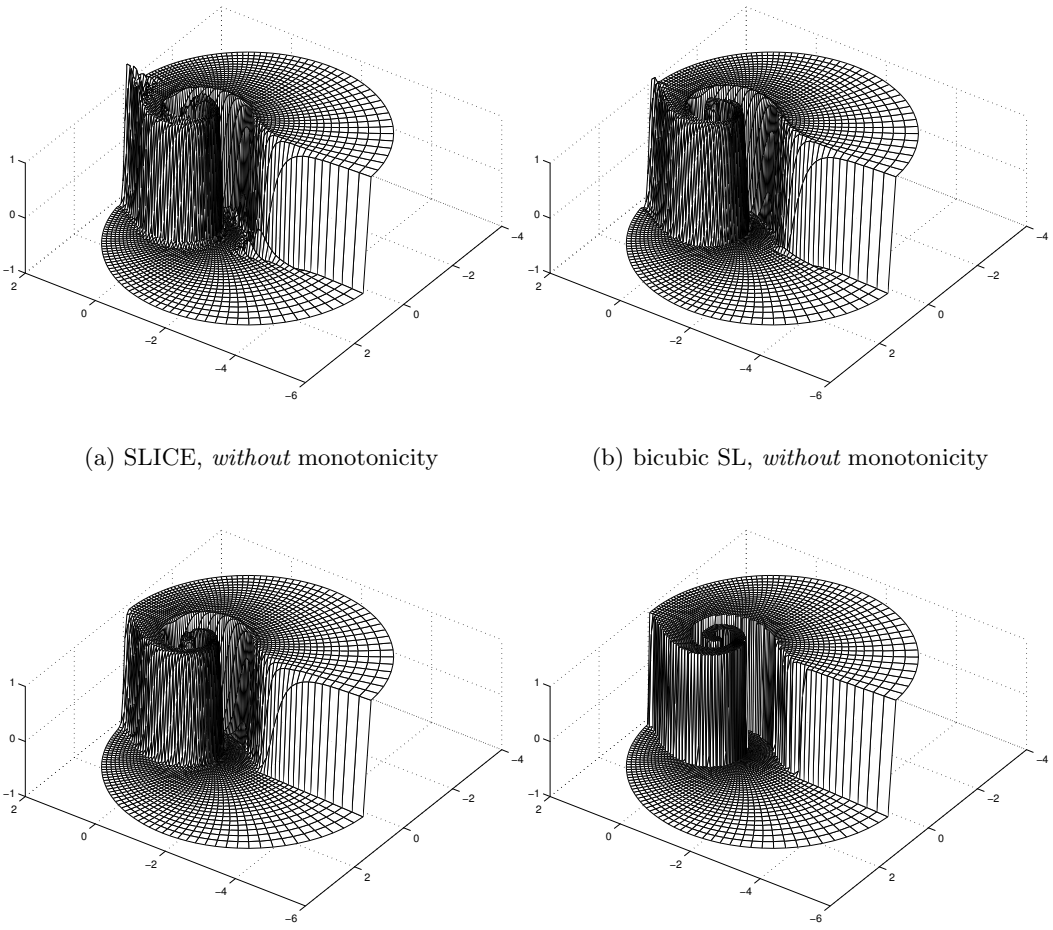

(a) SLICE, *without* monotonicity

(b) bicubic SL, *without* monotonicity

(c) SLICE, *with* monotonicity

(d) analytic

Figure 1: Solutions after 64 timesteps for non smooth deformational flow on a sphere - see Zerroukat et al. (2004) and Zerroukat et al. (2005) for definition of problem and parameters.

References

Purser, J. & Leslie, L. M. 1991 , An interpolation procedure for high-order three- dimensional semi-Lagrangian models, *Mon. Wea. Rev.* **119**, 2492–2498.

Zerroukat, M., Wood, N. & Staniforth, A. 2002 , SLICE: A Semi-Lagrangian Inherently Conserving and Efficient scheme for transport problems, *Q. J. R. Meteorol. Soc.* **128**, 2801–2820.

Zerroukat, M., Wood, N. & Staniforth, A. 2004 , SLICE-S: A Semi-Lagrangian Inherently Conserving and Efficient scheme for transport problems on the Sphere, *Q. J. R. Meteorol. Soc.* **130**, 2649–2664.

Zerroukat, M., Wood, N. & Staniforth, A. 2005 , A monotonic and positive-definite filter for a Semi-Lagrangian Inherently Conserving and Efficient (SLICE) scheme, *Q. J. R. Meteorol. Soc.* (to appear).